J. Fluid Mech. (1999), *vol.* 400, *pp.* 91–124. Printed in the United Kingdom

Dynamics and flow structures in the turbulent wake of rigid and flexible cylinders subject to vortex-induced vibrations

By CONSTANTINOS EVANGELINOS AND GEORGE EM KARNIADAKIS†

Division of Applied Mathematics, Brown University, Providence, RI 02912, USA

(Received 13 October 1998 and in revised form 25 June 1999)

We present simulation results of vortex-induced vibrations of an infinitely long flexible cylinder at Reynolds number $Re = 1000$, corresponding to a 'young' turbulent wake (i.e. exhibiting a small inertial subrange). The simulations are based on a new class of spectral methods suitable for unstructured and hybrid grids. To obtain different responses of the coupled flow–structure system we vary the structure's bending stiffness to model the behaviour of a vibrating inflexible (rigid) cylinder, a cable, and a beam. We have found that unlike the laminar flow previously studied, the amplitude of the cross-flow oscillation is about one diameter for the cable and the beam, close to experimental measurements, but is lower for the rigid cylinder. We have also found that for the latter case the flow response corresponds to parallel shedding, but for the beam and cable with free endpoints a mixed response consisting of oblique and parallel shedding is obtained, caused by the modulated travelling wave motion of the structure. This mixed shedding pattern which alternates periodically along the span can be directly related to periodic spatial variation of the lift force. In the case of structures with pinned endpoints a standing wave response is obtained for the cylinder; lace-like flow structures are observed similar to the ones seen in the laminar regime. Examination of the frequency spectra in the near wake shows that at $Re = 1000$ all cases follow a $-\frac{5}{3}$ law in the inertial range, which extends about half a decade in wavenumber. However, these spectra are different in all three cases both in low and high frequencies, with the exception of the beam and cable, for which the high-frequency portion is identical despite the differences in the displacement time history and the large-scale features of the corresponding flow.

1. Introduction

Fluid flows over flexible cylinders arise in many engineering situations, such as transmission lines, heat exchangers, marine cables towing instruments, flexible risers used in petroleum production and mooring lines, and other marine applications (see Blevins 1990; Vandiver 1991; Ramberg & Griffin 1976; Hover, Grosenbaugh & Triantafyllou 1994; Yoerger *et al.* 1991; Furnes 1998). It is important to understand the flow dynamics of the wake and be able to predict the hydrodynamic forces and motion of such structures caused by vortex-induced vibration (VIV). Simplified models rely on the force input as well as the added mass coefficient and correlation lengths (see Furnes 1998; Vandiver & Li 1994). From the fundamental point of view,

† Author for correspondence: e-mail: gk@cfm.brown.edu.

it is important to understand how the near wake is modified by the motion of the cylinder, which in turn depends on the flow conditions, the structural characteristics, and the type of support of the structure. While there has been significant progress in understanding the wake of a stationary cylinder in the last few years, especially in the low Reynolds number range (see Williamson 1996), there have been very few studies of the wake of freely oscillating cylinders (see Bearman 1984) with the emphasis placed primarily on the nonlinear dynamics of the structure, while modelling the wake as a simple oscillator (see Parkinson 1989).

In previous work, we have used direct numerical simulation to investigate laminar flow past a freely vibrating cable in three dimensions (see Blackburn & Karniadakis 1993; Newman & Karniadakis 1995, 1996, 1997). In particular, we employed a simple wave equation to model the motion of the structure, thereby neglecting the effect of bending stiffness. We found that, in the low Reynolds number regime we investigated, there are two possible states of the wake: one that corresponds to a travelling wave response, and another one that corresponds to a standing wave response. The first state produces a vorticity field consisting of oblique 'rollers' shed off the cylinder upper and lower surface. The second state corresponds to a three-dimensional staggered pattern forming lambda-type vortices. The existence of both states has been demonstrated recently by Olinger (1996), who used low-order modelling based on circle maps to represent shedding patterns behind flexible cables.

In these previous simulations, periodic boundary conditions were imposed on the side boundaries for both the flow and the structure. This configuration is an idealization, in essence, of a very long cable that is subject to spanwise disturbances of maximum wavelength determined by the imposed aspect ratio (length-to-diameter ratio L/d). In general, periodic boundary conditions seem to favour the travelling wave response in our simulations, but for low Reynolds numbers a standing wave one will persist for some time following a standing wave initial condition. Even in the case of a travelling wave initial condition, if the cable has a relatively small aspect ratio and is allowed to vibrate only in a cross-flow direction, the oblique shedding breaks down giving rise to a standing wave response.

Standing waves appear more naturally (even at higher Reynolds numbers) if the endpoints of the structure are pinned (i.e. fixed with all even derivatives of displacement equal to zero). The boundary conditions for the flow in this spanwise direction are still periodic. This configuration corresponds to a very long flexible cylinder supported by an array of fixed supports, uniformly distributed a distance L apart from each other.

Although standing wave patterns are more common in experimental situations, travelling wave responses have also been realized both in laboratory and field experiments, for example in the work of Alexander (1981), and in low Reynolds number experiments in the work of Van Atta, Gharib & Hammache (1988). Usually, travelling and standing wave patterns coexist, and this is also seen in the simulations. To document such a mixed response, we have simulated a relatively long cable ($\approx 100d$, where d is the diameter) with both of its endpoints pinned. The cable tension T and mass ratio ρ used were the same as for the simulations in Newman & Karniadakis (1997) (non-dimensional values of $T = 8.82$ and $\rho = 2$ respectively).

In figure 1 we plot the resulting response from the motion of the flexible cylinder, which was allowed to oscillate only in the cross-flow direction. We see that in regions close to the pinned endpoints a standing wave is developed, whereas in the mid-span a travelling wave appears with a symmetry line at the mid-point. We also see that due to constructive interference large amplitudes of $y/d \approx 1$ are obtained. This value

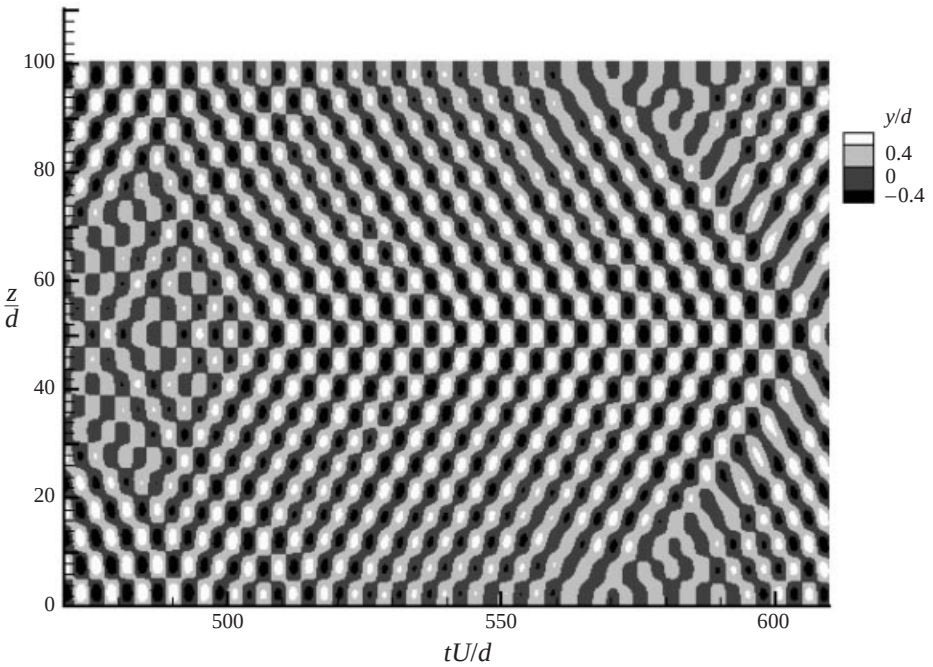

FIGURE 1. Flow past a freely vibrating flexible cylinder with pinned endpoints at $Re = 100$. Shown is the spanwise distribution of the amplitude of the cross-flow motion versus time. For clarity isocontours at $y/d = \pm 0.4$ are used which are far below the maximum value of 1 observed. The chessboard pattern corresponds to a standing wave response and the parallel lines to a travelling wave one.

should be contrasted with the 'free' periodic ends case, which gives a maximum amplitude of $y/d \approx 0.5d$–$0.6d$ at this Reynolds number ($Re = 100$) (see Newman & Karniadakis 1997). More specifically, the amplitude of about $0.5d$–$0.6d$ is obtained for laminar flow irrespective of the response, i.e. travelling or standing wave, although the lift force in the former case is less than half of the lift force of the latter. This result points to the importance of the phase difference between the motion and the lift force, the selection of which is based on a subtle and yet unexplained coupling mechanism between the near-wake dynamics and the structure dynamics.

Another important factor that affects the coupled flow–structure response is the structural characteristics, i.e. damping and bending stiffness. The case of zero structural damping results in the maximum response at resonant (lock-in) conditions. The elasticity of the structure, on the other hand, determines the excited modal shape. Therefore, a tension-dominated cable with zero bending stiffness will respond differently than a beam with finite bending stiffness even at lock-in conditions. In laminar states, both structures and the resulting flow pattern are identical as the only excited mode is the first one. However, at higher Reynolds number in the transitional and turbulent flow states, a multi-modal response is obtained. Therefore, even if the first mode dominates the response, excitation of higher modes of the structure is possible, giving rise to significant differences in the topology and dynamics of the near wake. For long cables, high modes usually dominate the response and thus the effect of bending stiffness cannot be neglected (see Furnes 1998). In engineering practice, a simple criterion has been developed to decide what type of modelling is to be used (see Vandiver 1991). For example, a structure can be modelled as *a cable* if it is

tension-dominated, i.e. $T/(EIk^2) > 30$, otherwise it is modelled *as a beam* and its bending stiffness should be taken into account. Here T is the tension, EI the bending stiffness, and k is the wavenumber describing the excitation mode.

In the current work, we investigate the physics of VIV in a simplified setting, one which is computationally convenient but still maintains the main engineering features. In particular, we consider long flexible cylinders, which we will model as linear cables and beams subject to resonant VIV at Reynolds number $Re = 1000$, which is one order of magnitude higher than the one considered in our previous work (Newman & Karniadakis 1997). At this Reynolds number flow past a stationary cylinder gives rise to a turbulent wake (see Williamson 1996). While some experimental evidence suggests that for $Re \geqslant 500$ there are no significant Reynolds number effects (see Vandiver 1991), more recent experiments by Ching, So & Zhou (1998) and our simulations suggest otherwise. A further simplification is that we only consider here the dominant motion which is in the cross-flow direction; that is, we neglect the amplitude of the streamwise motion, which is typically 10% to 15% of the amplitude in the cross-flow motion. Finally, since we are interested in the maximum possible response we neglect the effect of structural damping.

The specific questions we address are the following.

What is the maximum amplitude response of cables, beams and rigidly vibrating cylinders in the 'young' turbulent regime, and how does it compare with the response in the laminar flow regime?

What is the phase difference between structure motion and lift forces, and what flow features determine the selection process?

What are the excited structural modes, and what flow structures are responsible for a multi-modal excitation in the turbulent regime?

What are the qualitative and quantitative differences between the turbulent wake of a stationary cylinder and the wakes behind freely vibrating rigid cylinders, and flexible cables and beams?

To address these questions, we use direct numerical simulation based on a new spectral method that employs unstructured grids and dynamic refinement. In § 2 we summarize the simulation parameters, and we include more details of the simulation and the method in Appendix A. In § 3 we present results for the vibration amplitude and lift force time histories as well as their phase difference. In § 4 we present statistics of the turbulent near wake and of the structure, and in § 5 we present representative flow visualizations, with a discussion of the visualization methodology employed in Appendix B. We conclude with a discussion in § 6.

2. Simulation parameters

We report here simulation results at Reynolds number $Re = 1000$ and mass ratio (cylinder mass over displaced fluid mass) $\rho = 2$, which is a representative value for VIV in water. The Reynolds number is defined based on the cylinder diameter d and the free-stream velocity U. In all cases we neglect the structural damping as we are interested in the maximum amplitude response. We also allow only vertical motions in the crossflow y-direction, i.e. we do not allow any motion in the streamwise x-direction. We have chosen the structure eigenfrequency to be approximately equal to $2\pi St$ (where St is the Strouhal number of the corresponding stationary cylinder flow) as we are interested in lock-in states only. Deviations from this resonant state and transition to quasi-periodic states have also been studied in Evangelinos (1999).

The governing equations are the incompressible Navier–Stokes equations cou-

pled with the equation of the structure dynamics. All of our variables are non-dimensionalized using the cylinder diameter d and the inflow velocity U. In the following, we will refer to a *cable* as the structure whose dynamics is described by

$$\frac{\partial^2 y}{\partial t^2} = c^2 \frac{\partial^2 y}{\partial z^2} + \frac{F_y}{\rho} \Longleftrightarrow \frac{\partial^2 \hat{y}_m}{\partial t^2} = -\Omega^2 m^2 \hat{y}_m + \frac{\hat{F}_y}{\rho} \tag{2.1}$$

in physical and Fourier space (Fourier series expansion in terms of $e^{i(2\pi/L)mz}$), respectively. Here, m is the Fourier mode, $c^2 = T/\rho$ and $\Omega = c2\pi/L$; for our simulations $L = 4\pi$ is the length of the cable in the equilibrium position. Thus, to establish lock-in for the mth mode of oscillation, we choose $\Omega m \approx 2\pi St$. F_y here is the total lift force, i.e. the sum of pressure and viscous forces exerted by the fluid on the structure in the y-direction.

Similarly, we will refer to a *beam* as the structure whose dynamics is described by

$$\frac{\partial^2 y}{\partial t^2} = -\gamma^2 \frac{\partial^4 y}{\partial z^4} + \frac{F_y}{\rho} \Longleftrightarrow \frac{\partial^2 \hat{y}_m}{\partial t^2} = -\Omega^2 m^4 \hat{y}_m + \frac{\hat{F}_y}{\rho} \tag{2.2}$$

in physical and Fourier space, respectively. Here, $\gamma^2 = EI/\rho$ and $\Omega = \gamma(2\pi/L)^2$. Again, to establish lock-in for the mth mode, we choose $\Omega m^2 \approx 2\pi St$. Thus for $m = 1$ both the cable and the beam cases at lock-in reduce to $\Omega \approx 2\pi St$ and so the necessary conditions for a cable with tension T and a beam of bending stiffness EI to exhibit lock-in at this mode are

$$c \approx LSt \Longrightarrow T \approx \rho L^2 St^2, \tag{2.3a}$$

$$\gamma \frac{2\pi}{L} \approx LSt \Longrightarrow EI \approx \tfrac{1}{4}\rho \frac{L^4}{\pi^2} St^2. \tag{2.3b}$$

In the case of the pinned endpoints we use a Fourier sine expansion (in terms of $\sin((\pi/L)mz)$) for the structure's displacement. This expansion automatically satisfies the boundary conditions. This gives $\Omega = c(\pi/L)$ and $\Omega = \gamma(\pi/L)^2$ for the cable and the beam respectively and (2.3) becomes

$$c \approx 2LSt \Longrightarrow T \approx 4\rho L^2 St^2, \tag{2.4a}$$

$$\gamma \frac{\pi}{L} \approx 2LSt \Longrightarrow EI \approx 4\rho \frac{L^4}{\pi^2} St^2. \tag{2.4b}$$

The coupled Navier–Stokes/structure dynamics equations are discretized in space using a new spectral method that employs a hybrid grid in the (x, y)-plane and Fourier complex exponentials in the z-direction (cylinder axis). The parallel code $\mathcal{N}\boldsymbol{\epsilon\kappa}\mathcal{T}\boldsymbol{\alpha r}$ written in $C++$ and MPI is employed in all simulations (see Warburton 1998). A boundary-fitted coordinate system is employed similar to the laminar flow simulations in Newman & Karniadakis (1997), which has been validated against an arbitrary Lagrangian Euler (ALE) formulation (see Evangelinos 1999) that we have also developed for moving domains (see Warburton & Karniadakis 1997). The computational domain is shown in Appendix A in figure 28 where more details can be found about the numerical method.

3. Spatio-temporal variation of amplitude, lift and drag

The *self-limiting* behaviour of VIV as the damping goes to zero has been well documented by the various experimental data compiled by Griffin (1992) and was

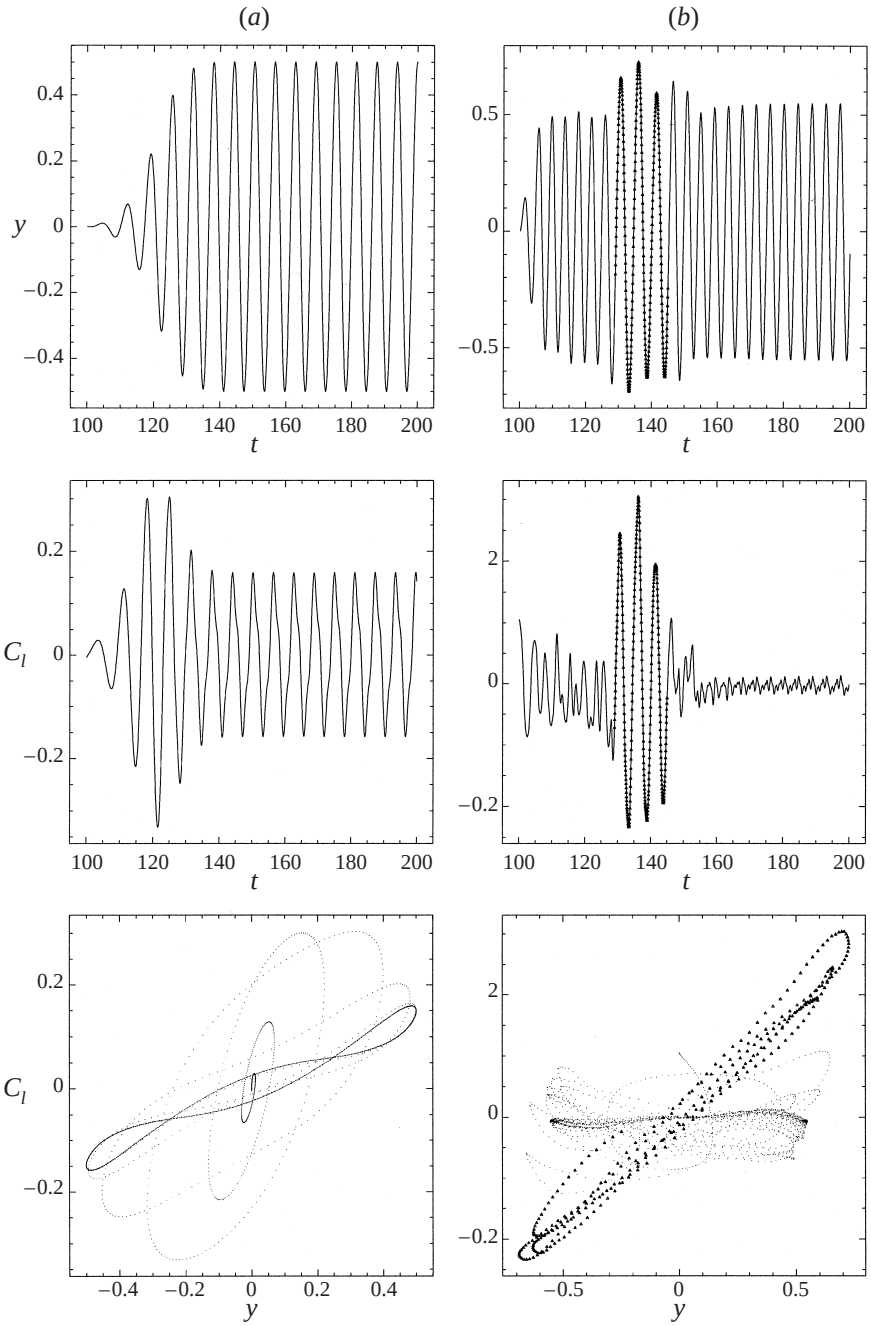

FIGURE 2. Two-dimensional simulations at $Re = 100$ (*a*) and $Re = 1000$ (*b*). Top: cross-flow displacement history; middle: lift coefficient history; bottom: phase portrait. All quantities are non-dimensionalized. The black triangles mark the transient stage where the lift and the displacement are oscillating in phase.

also reproduced in the simulations of Newman & Karniadakis (1997). More specifically, the simulations in the latter were for low Reynolds number ($Re \leqslant 200$) and (especially the two-dimensional simulations) underpredicted the maximum amplitude

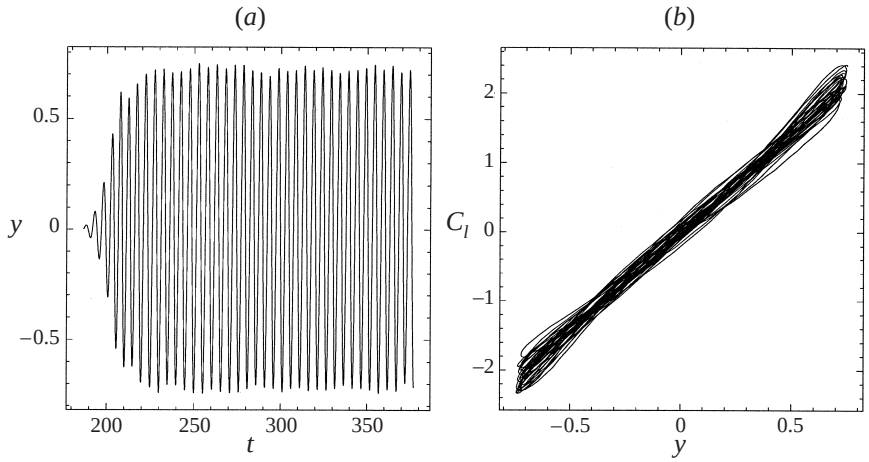

FIGURE 3. Rigid cylinder: cross-flow displacement versus time (*a*) and span-averaged lift coefficient versus cross-flow displacement (*b*). All quantities shown are non-dimensionalized.

at zero damping. Here, we first examine possible Reynolds number effects in the two-dimensional simulations, by simulating lock-in states at $Re = 100$ and $Re = 1000$ but otherwise identical conditions.

In figure 2 we plot the results from these two-dimensional simulations. We see that asymptotically (after the transients die out) approximately the same response is produced in both simulations. More specifically, a small increase of less than 10% in the amplitude is observed as we increase the Reynolds number from $Re = 100$ to $Re = 1000$. We also note that in the case of $Re = 1000$ a sudden increase in the amplitude is associated with a corresponding increase of the lift coefficient and a jump in phase between those two quantities. During this transient stage the lift force and the cross-flow amplitude are in phase, as shown in the bottom plot of figure 2, and the amplitude reaches values of $0.7d$. The two-dimensional simulations at higher Reynolds number underpredict significantly the maximum amplitude response at zero structural damping which according to the experiments is $y/d \approx 1$ (see Griffin 1992). As regards the frequency response, at $Re = 100$ the input (non-dimensional) frequency, i.e. the structure eigenfrequency, was set to $f_n = 0.167$, which is equal to the Strouhal frequency of the stationary cylinder flow at the same Reynolds number. The resulting (non-dimensional) structure frequency and wake frequency obtained from the simulation were 0.163 and 0.160, respectively. Similarly, at $Re = 1000$ the input frequency was set to 0.238 and the structure and wake frequency obtained from the simulation was 0.238. Therefore, for these two-dimensional simulations if the structure eigenfrequency matches the Strouhal frequency of the corresponding stationary flow, the frequency of the coupled system deviates very little. We will see that this is not the case for the three-dimensional simulations.

3.1. *VIV of a rigidly moving cylinder*

In the following we will concentrate exclusively on three-dimensional simulations. First, we present results from simulations of flow past a rigid cylinder at $Re = 1000$ subject to VIV. We see in figure 3(*a*) that a slightly modulated harmonic motion is produced with maximum amplitude $y/d \approx 0.74$, which is larger than the corresponding value of the two-dimensional simulation of $y/d \approx 0.55$. This motion is in phase with

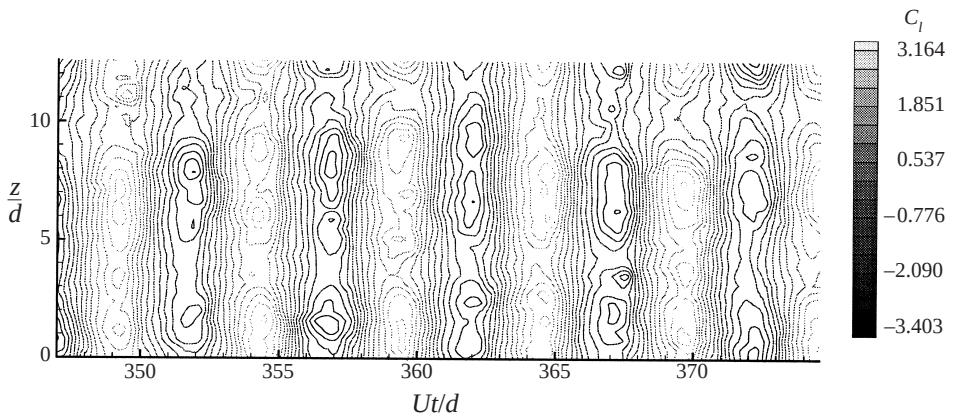

FIGURE 4. Rigid cylinder: lift coefficient along the span versus time.

the span-averaged lift coefficient as revealed in the phase portrait shown in figure 3(*b*) in agreement with the experiments of Brika & Laneville (1993). Note that in the two-dimensional motion (see figure 2) the same large amplitude is obtained during the transient short period when the lift coefficient is in phase with the cross-flow motion (between times 130 and 140 non-dimensional time units). Correspondingly, the values of the two-dimensional (during that transient period) and span-averaged three-dimensional lift coefficient are also close.

The lock-in state of the freely oscillating rigid cylinder is described by a two-branch response as documented in the detailed experiments of Brika & Laneville (1993) and Khalak & Williamson (1996): an upper branch that corresponds to large amplitude and low values of reduced velocity, and a lower branch that corresponds to low amplitudes and large values of the reduced velocity. A similar result was also obtained by Hover, Techet & Triantafyllou (1998) at a Reynolds number $Re = 3800$, which is lower than that in Khalak & Williamson (1996) but at comparable (small) values of the structural damping. The classical results of Feng (1998) were obtained for relatively large damping (see also Brika & Laneville 1993) but they show essentially the same response at reduced levels. By comparing the numerical results here with both sets of recent experiments, it appears that the three-dimensional simulations capture the upper branch corresponding to an oscillation in phase with the lift coefficient. There is also agreement in the amplitude of oscillation with the experimental data, especially with the data of Hover *et al.* (1998), which having been obtained at $Re = 3800$ are closer to the Reynolds number in our simulation. On the other hand, it seems that the two-dimensional simulations capture the lower branch of the amplitude response curve corresponding to an oscillation which is not phase-synchronized with the lift force as shown in figure 2. This observation was first made by Khalak & Williamson (1996) in comparing their experimental data with two-dimensional simulations reported in Newman & Karniadakis (1995).

The rigid cylinder is allowed to oscillate only in the cross-flow direction and therefore the motion is uniform along its axis. However, the corresponding flow is strongly three-dimensional as shown by the spanwise distribution of lift coefficient in figure 4. It exhibits strong cellular structure with peaks exceeding the peaks of the span-averaged coefficients by almost 50%.

As regards the frequency response, the input non-dimensional frequency was 0.238, equal to the Strouhal frequency of the two-dimensional cylinder wake at $Re = 1000$.

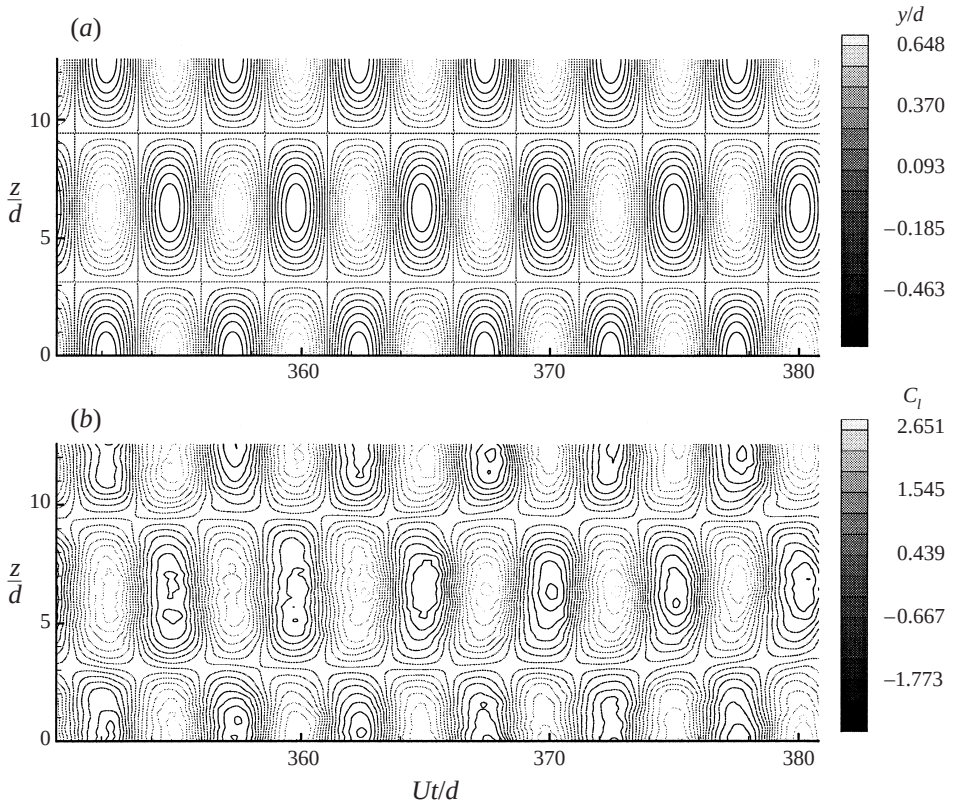

FIGURE 5. Flexible cylinder subject to forced oscillation: standing wave pattern (*a*) and lift coefficient (*b*).

The resulting structure frequency (obtained from the spectrum of the cross-flow motion) was 0.197 and the wake frequency was 0.201. Note that the Strouhal frequency of the corresponding three-dimensional wake is 0.202. We see therefore here that the coupled structure–flow system has a frequency response that greatly deviates from the imposed frequency of the structure (here 0.238). This non-classical result has also been reported in experimental studies recently by Gharib *et al.* (1998) and it was found to be a function of the mass ratio; for large values of mass ratio the frequency response approaches the classical lock-in behaviour.

3.2. *Flow past a flexible cylinder in prescribed motion*

To identify differences in forces due to the cylinder deformation only, we simulated next a flexible cylinder subject to prescribed cross-flow vibrations corresponding to a standing wave pattern as shown in figure 5. The amplitude of the oscillation is set to match the amplitude of the free oscillation of the rigid cylinder at $Re = 1000$, and the frequency is set to 0.197, close to the Strouhal frequency of a stationary cylinder and equal to the frequency that the rigid cylinder in § 3.1 freely vibrated at. The lift force is in phase with the cylinder cross-flow motion as shown in figure 5, and the maximum amplitude of the lift coefficient is lower than the free-oscillating rigid cylinder by about 20%.

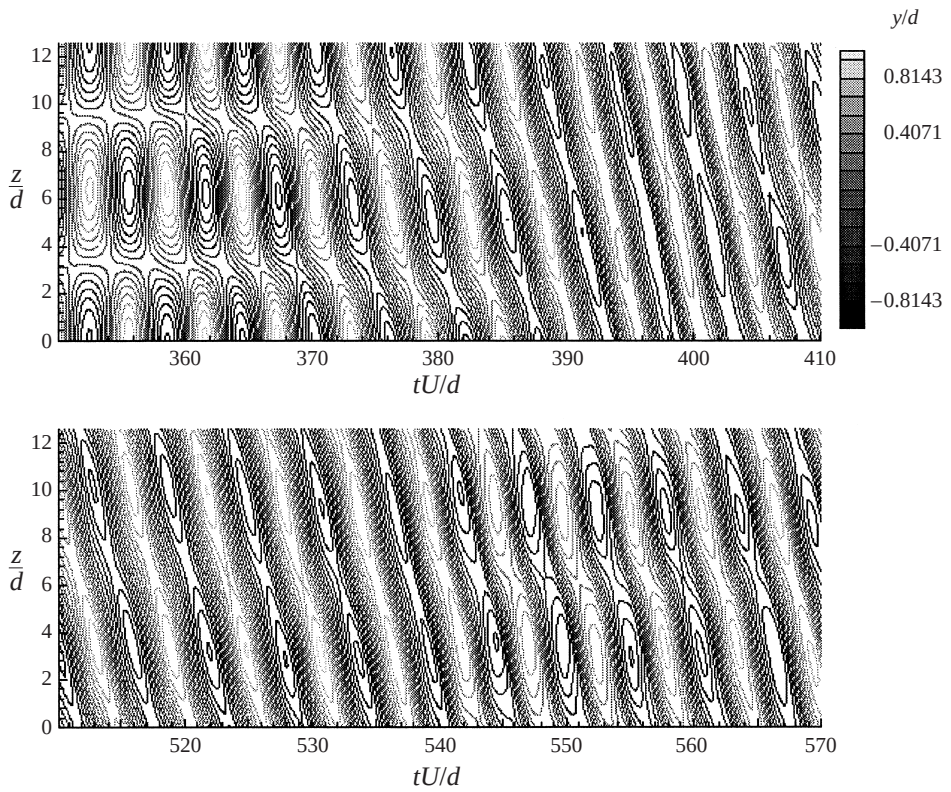

FIGURE 6. Cable: cross-flow displacement along the span versus time. The initial part of the simulation is shown at the top and a later part at the bottom.

3.3. *VIV of a cable*

For the free periodic boundaries that we use, the standing wave response is not a stable state if the cylinder motion is due to vortex shedding (VIV) and not a prescribed motion. This was also shown to be the case for the laminar wake at $Re = 100$ (see Newman & Karniadakis 1997), where an initial standing wave response, typically although not always, turns into a travelling wave response. The details of the motion depend on the type of structure at high Reynolds number, and in particular its bending stiffness; this structural dependence is exhibited only in the transitional and turbulent wakes. We examine this issue first by considering the cylinder as a flexible cable and modelling its dynamics by a wave equation (2.1).

The initial conditions correspond to the case of the forced standing wave pattern discussed in § 3.2. In figure 6 we plot the cross-flow displacement along the span as a function of time. We see that the standing wave response turns into a modulated travelling wave response after approximately 5 shedding cycles. Therefore, the coupled cable–flow response in the 'young' turbulent regime at $Re = 1000$ is qualitatively similar to the response at laminar conditions at an order of magnitude lower in Reynolds number (see Newman & Karniadakis 1997). However, the travelling wave in the turbulent state is subject to significant modulation unlike the laminar case. We will discuss the corresponding flow structures in § 5. The cross-flow oscillation amplitude reaches values of $1d$ in the initial stages, during the transition from standing to travelling wave, and maintains values as high as $0.9d$ and slightly higher afterwards.

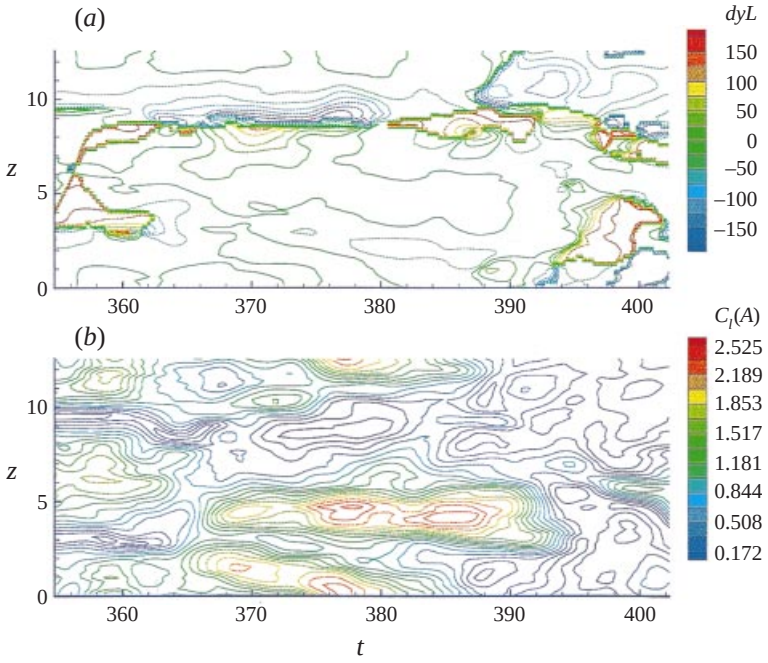

FIGURE 7. Cable–demodulation analysis: phase difference between the cross-flow displacement and the lift coefficient (*a*); amplitude of the lift coefficient (*b*). The sharp discontinuities are due to the fact that individual phases are calculated modulo 180° before their difference is calculated (also modulo 180°).

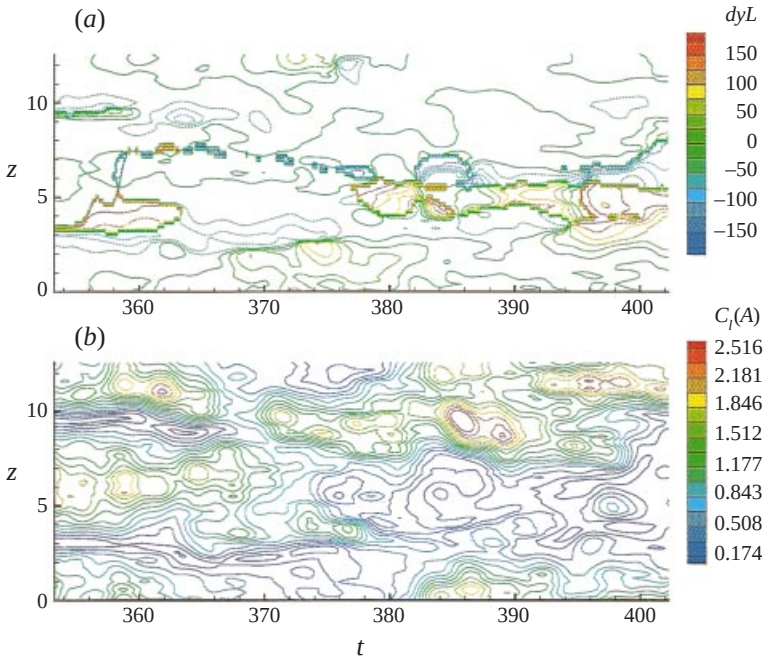

FIGURE 9. Beam–demodulation analysis: phase difference between the cross-flow displacement and the lift coefficient (*a*), and the amplitude of the lift coefficient (*b*).

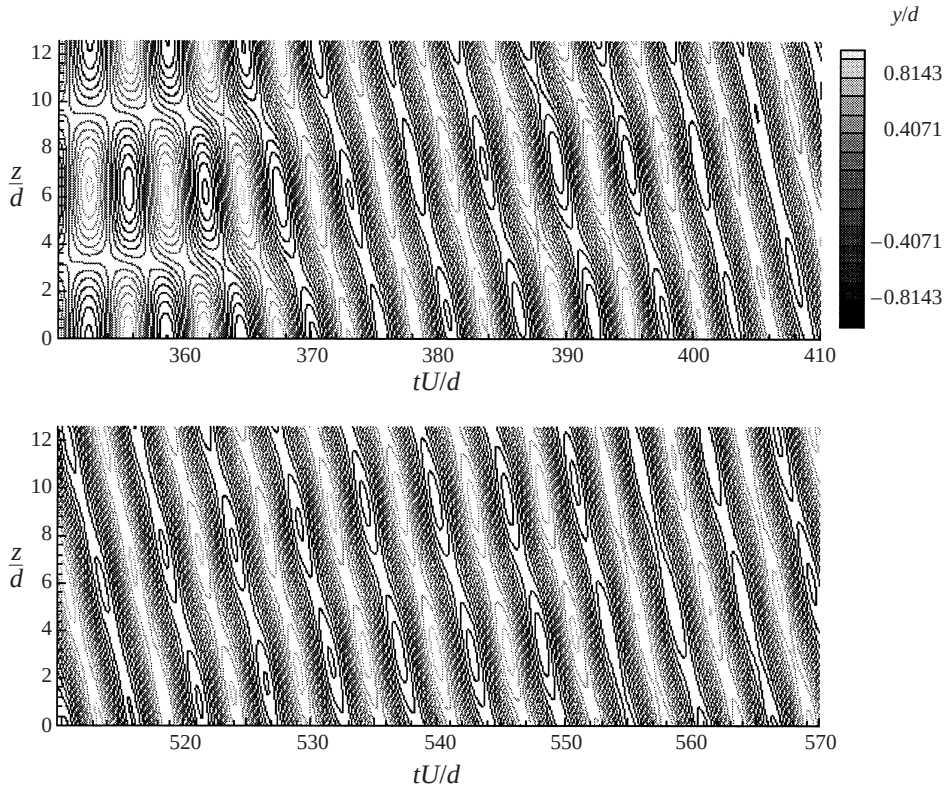

FIGURE 8. Beam: cross-flow displacement along the span versus time. The initial part of the simulation is shown at the top and a later part at the bottom.

Unlike the previous cases where we found that the lift coefficient and the cross-flow displacement are essentially in phase, in the case of the freely vibrating cable this is not true. To quantify this phase difference we employ *complex demodulation analysis*, which is a more general approach than harmonic analysis in dealing with non-exact periodic time series (see Bloomfield 1976). A complex demodulation of a time series $S(t_n)$ with a dominant frequency component λ will give a time-varying amplitude $R(t)$ and phase $\Phi(t)$ such that

$$S(t_n) \approx R(t_n)\mathrm{e}^{\mathrm{i}(\lambda t_n + \Phi(t_n))}. \tag{3.1}$$

In figure 7 we plot the amplitude $R(t)$ of the lift coefficient and its phase difference with respect to the cylinder displacement. We see that there is a very strong correlation between regions of almost zero phase difference and maximum amplitude in the lift coefficient. However, and unlike the previous cases, there are also regions with large phase differences between the lift forces and the cable motion. As regards the frequency response, here the input (non-dimensional) frequency was set to 0.197, close to the Strouhal frequency of the corresponding stationary three-dimensional wake and equal to the frequency that the rigid cylinder in § 3.1 freely vibrated at. The resulting frequencies of the structure and wake were 0.176 and 0.1876, respectively, again deviating from the classical lock-in response, in agreement with the findings in Gharib *et al.* (1998).

3.4. *VIV of a beam*

Next, we examine the response of a beam, i.e. a structure with finite bending stiffness, under identical conditions as in the cable case discussed above, including the same initial conditions. The bending stiffness is chosen using (2.3) so that the same structural mode $m = 1$ as before is mainly excited. We see again from the simulations that the initially prescribed standing wave response turns into a modulated travelling wave response as in the cable case, but the path of transition as well as the asymptotic state are different. Therefore, different spanwise modes are excited in the beam case compared to the cable case as can be seen by comparing (2.1) and (2.2) in Fourier space. In figure 8 we plot the cross-flow displacement versus time, and we see this transition from a standing to a modulated travelling wave response. However, we also observe clear differences with the corresponding plot for the cable in figure 6. Again, the cross-flow amplitude reaches values of $1d$ in the initial (transitional) stages and maintains values over $0.8d$ afterwards. For both the cable and beam cases, the $1d$ amplitude reached is much larger than the $0.74d$ of the initial conditions of the simulations – this indicates that amplitudes of that size are possible at $Re = 1000$.

To quantify the phase difference between the beam motion and the corresponding lift coefficient, we employ again complex demodulation analysis to construct the plot in figure 9 for the amplitude of the lift coefficient and its phase difference with respect to the motion. We see that the maximum lift coefficient is subject to very large modulation following the large variation in phase difference. For example, regions of small phase difference (less than 10°) result in values of maximum lift coefficient of more than $C_l \approx 2$ but phase differences of 90° or higher are also possible leading to lift coefficient amplitudes of less than $C_l \approx 0.5$. As regards the frequency response, the input frequency was set to 0.197 as in the case of the cable, and the resulting structure and wake frequencies were 0.178 and 0.1736, respectively.

3.5. *VIV of a bean with pinned endpoints*

To investigate the effect of the boundary conditions for the structure, we also simulated flow past a flexible beam (with the same length and structural caracteristics as in § 3.4) with pinned endpoints ($y = y'' = 0$).

In figure 10(*a*) we plot the cross-flow displacement of the pinned beam versus time. A stable asymptotic standing wave response is observed, and we see that the maximum amplitude is more than one cylinder diameter, and in fact about 20% higher than the asymptotic travelling wave response seen in § 3.4. In figure 10(*b*) we plot the corresponding lift coefficient distribution. The lift variation is again large, displaying a clear standing wave pattern.

4. Correlation length and spectra

4.1. *Autocorrelation functions*

In studies of VIV the value of spanwise correlation length is very important as many empirical models rely on it (see Blevins 1990). However, related studies and experimental measurements are relatively few (see Toebes 1969; Ramberg & Griffin 1976). For stationary cylinders, detailed measurements of correlation length based on the autocorrelation function were obtained only recently by Mansy, Yang & Williams (1994). We define here the autocorrelation function as follows:

$$R_{uu}(l; x, y) = \frac{\overline{u(x, y, z, t)u(x, y, z - l, t)}}{\overline{u^2(x, y, z, t)}}, \tag{4.1}$$

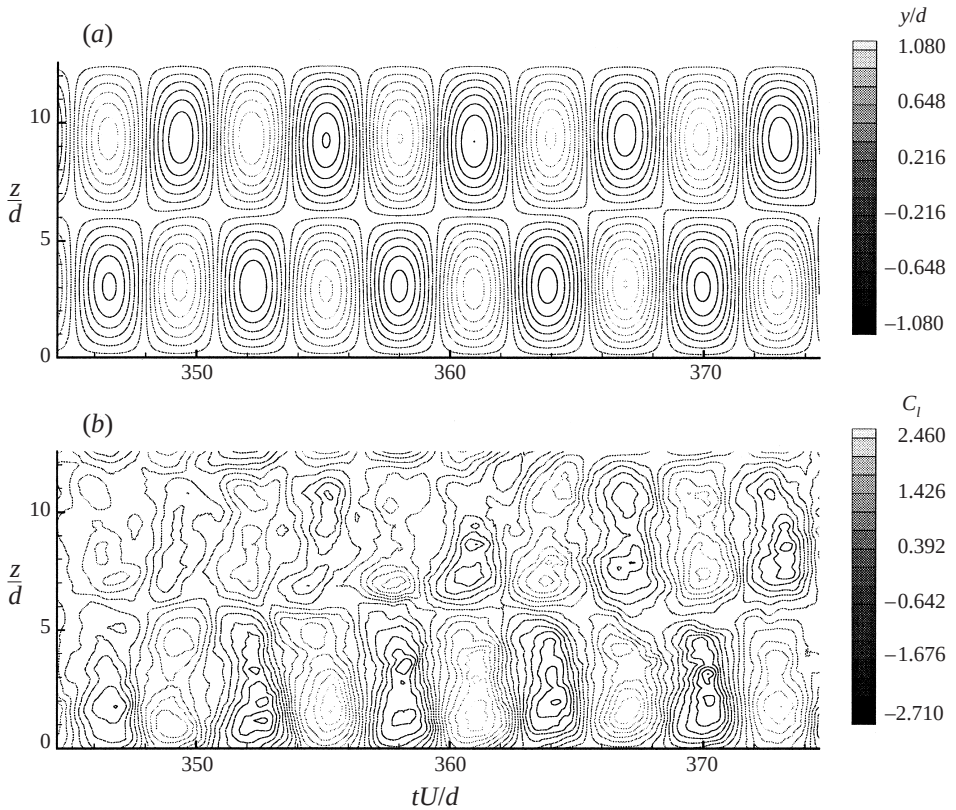

FIGURE 10. Beam with pinned endpoints: cross-flow displacement (*a*) and lift coefficient (*b*) along the span versus time.

where the bar denotes averaging over time and over z-planes. Also, $u(x, y, t)$ is the fluctuation obtained after we subtract the mean quantity, i.e. averaged in time t and span z at the (x, y) point.

In figures 11 and 12 we plot the absolute value of the autocorrelation function for two points in the near wake for the streamwise and cross-flow components of velocity. One point is on the centreline ($x/d = 3$; $y/d = 0$) and the other is one cylinder diameter above it ($x/d = 3$; $y/d = 1$). We include results for a stationary and a freely oscillating rigid cylinder, a cable and a beam. Results for the spanwise component of velocity can be found in Evangelinos (1999).

These results are in good agreement with the results of Toebes (1969) for oscillating rigid cylinders, and of Mansy *et al.* (1994) for stationary cylinders. In particular, the oscillatory structure in $|R_{uu}|$ (see figure 11) for a stationary cylinder was also shown in the work of Mansy *et al.* (1994). The autocorrelation function $|R_{vv}|$ (see figure 12) indicates a high degree of correlation for the rigidly oscillating cylinder, consistent with the experimental observations (Toebes 1969; also, M. S. Triantafyllou, private communication).

Looking at the behaviour of the autocorrelation functions $|R_{uu}|$ and $|R_{vv}|$ in more detail we note the following.

(i) The R_{uu} for the cable and beam at the centreline point become negative (hence the 'cusp' in the $|R_{uu}|$ graph) at approximately the mid-quarter spanwise location in agreement with the experimental measurements of Ramberg & Griffin (1976). For

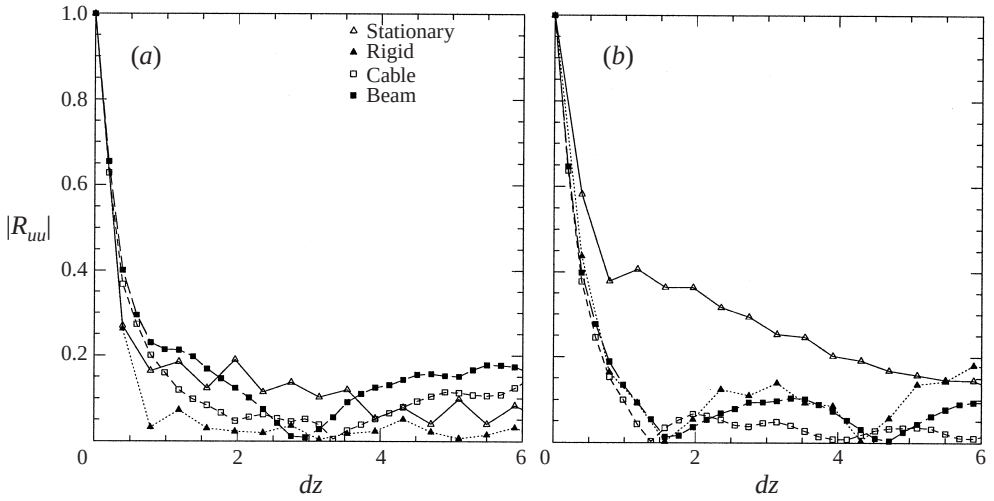

FIGURE 11. Autocorrelation function for the streamwise component of velocity in the near wake at a centreline point ($x/d = 3;\ y/d = 0$) (*a*) and an off-centreline point ($x/d = 3;\ y/d = 1$) (*b*). The distance dz is non-dimensionalized with the cylinder diameter d.

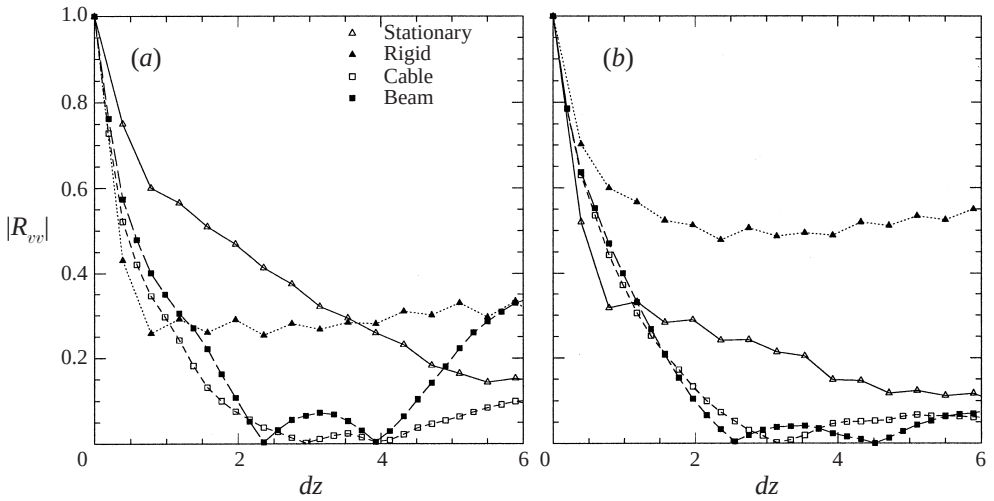

FIGURE 12. Autocorrelation function for the cross-flow component of velocity in the near wake at a centreline point ($x/d = 3; y/d = 0$) (*a*) and an off-centreline point ($x/d = 3; y/d = 1$) (*b*). The distance dz is non-dimensionalized with the cylinder diameter d.

off-centreline locations, the rigidly oscillating cylinder displays the same behaviour as the two flexible structures, with two crossings of the horizontal axis at $L/8$ and $3L/8$. In this case the actual value for the cable $|R_{uu}|$ is very small, with slightly larger values for the beam.

(ii) For the stationary cylinder $|R_{uu}|$ and $|R_{vv}|$ decay about equally slowly for the off-centreline point. In the case of the centreline point though, $|R_{uu}|$ decays rapidly while $|R_{vv}|$ decays even more slowly than in the case of the off-centreline point.

(iii) The rigidly moving cylinder exhibits large values of $|R_{vv}|$ for both points (relatively larger in the case of the off-centreline one) – the function (as expected) does not tend to zero.

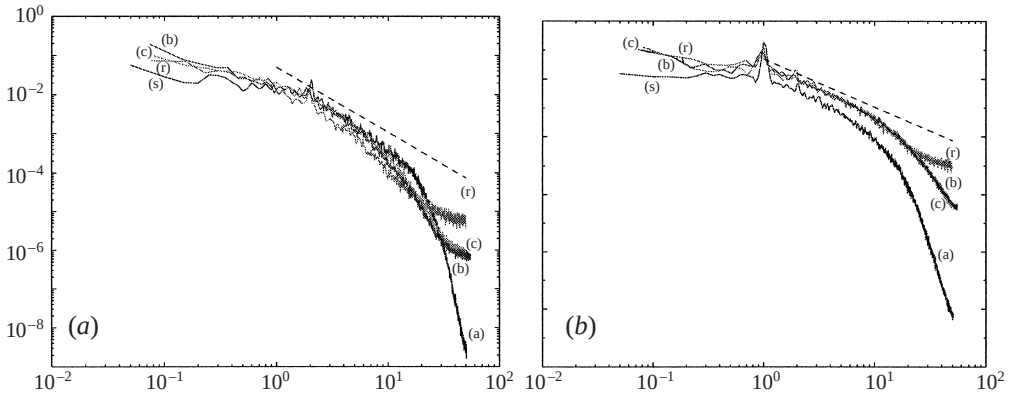

FIGURE 13. Energy spectra (streamwise velocity) for stationary (s), freely oscillating rigid cylinder (r), cable (c) and beam (b) at a point in the wake at centreline ($x/d = 3, y/d = 0$) (*a*) and off-centreline ($x/d = 3, y/d = 1$) (*b*).

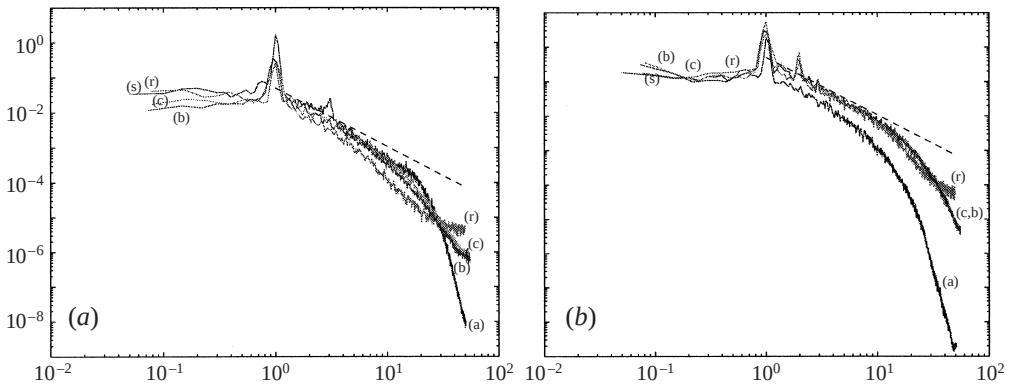

FIGURE 14. Energy spectra (cross-flow velocity) for stationary (s), freely oscillating rigid cylinder (r), cable (c) and beam (b) at a point in the wake at centreline ($x/d = 3, y/d = 0$) (*a*) and off-centreline ($x/d = 3, y/d = 1$) (*b*).

(iv) The cable and the beam R_{vv} values initially decay similarly but cross the horizontal axis at slightly different locations for the first time (the cable values around $L/4$, the beam at a lesser value). For larger dz values, both of them cross the axis again for the centreline point but this is not so for the off-centreline one in the case of the cable. The beam values for the centreline point reach the level of those of the rigidly moving cylinder for larger dz while the cable values stay small.

We note again that there is greater similarity between the R_{uu} values for the cable and the beam than for the corresponding R_{vv} ones; it is not clear to us at present why there is such a discrepancy.

4.2. *Spectra of the velocities in the near wake*

Next, we turn our attention to the pointwise statistics focusing on both the near wake as well as the structure itself. First, we present energy spectra obtained at the points $(x/d, y/d) = (3, 0)$ (centreline) and $(x/d, y/d) = (3, 1)$ (off-centreline) for a stationary and a freely oscillating rigid cylinder, a cable and a beam.

In figure 13 we plot the results of the streamwise velocity signal by normalizing the frequency with the corresponding dominant frequency of the near wake for each

case. In figure 14 we plot the corresponding results for the cross-flow velocity; data for the spanwise component can be found in Evangelinos (1999). We see that even at this relatively low Reynolds number of $Re = 1000$ an inertial subrange of about half a decade or more in wavenumber has been established. For the stationary cylinder, scales which are higher than 10 times the Strouhal frequency are rapidly decaying; however for the rigid cylinder even high-frequency components are very energetic, with the cable/beam ones somewhat less energetic. We note the following.

(i) For the centreline point:
only the cross-flow velocity spectra exhibit a sharp peak at the Strouhal frequency; the inertial range for the stationary cylinder is the widest, and for at least half a decade the spectrum for the beam and the cable is at the same level, with that of the rigidly moving cylinder slightly below; in the smallest scales, the situation is reversed.

(ii) For the off-centreline point:
all velocity spectra exhibit a sharp peak at the Strouhal frequency; the inertial range for the rigidly moving cylinder, cable and beam appears to be common, except for the case of the cross-flow velocity where the rigidly moving cylinder spectrum falls off the $-\frac{5}{3}$ slope first; in all cases the spectrum for the stationary cylinder is below that of all the other cases past the Strouhal frequency; the cross-flow velocity spectrum exhibits a strong $2f$ superharmonic response for all the moving structure cases.

4.3. *Excitation of the structural modes*

It is clear from the results presented above that the cable–flow response is substantially different from the beam–flow response at this Reynolds number ($Re = 1000$), despite the fact that the scaled wake velocity spectra of the beam and cable wakes were shown to be almost identical. At lower Reynolds number, i.e. $Re = 100$, the responses are identical as the only excited mode is the first one ($m = 1$) (Newman & Karniadakis 1997). We have found in our simulations (see Evangelinos 1999) that for $100 \leqslant Re \leqslant 200$ a transition takes place for the cable–flow system and other modes, in addition to the first one, are excited although at reduced levels. However, for the beam–flow system this transition takes place at substantially higher Reynolds number ($Re_c \geqslant 500$) although we could not bracket exactly the critical value.

At the $Re = 1000$ that we study here we have decomposed the amplitude of the vibration into Fourier modes along the spanwise direction. In figure 15 we plot the amplitude of the first four modes of the cable motion versus time. We see that although the first mode dominates, the other three modes contribute a non-negligible amount to the energy, with the second and third mode almost at the same level. The same type of decomposition is shown in figure 15 for the beam, with the important difference that here all modes are clearly separated and at reduced levels compared to the cable modes. This is consistent with our aforementioned finding that the critical Reynolds number for transition is lower for the cable than for the beam.

5. Flow visualizations

5.1. *Two-dimensional simulations*

We first examine flow structures present in the two-dimensional simulations at $Re = 1000$. As we can see from the variation of lift as a function of time in figure 2 there are two distinct states that the flow goes through before it reaches its asymptotic state. (The initial conditions at $t = 100$ correspond to a converged flow past a stationary

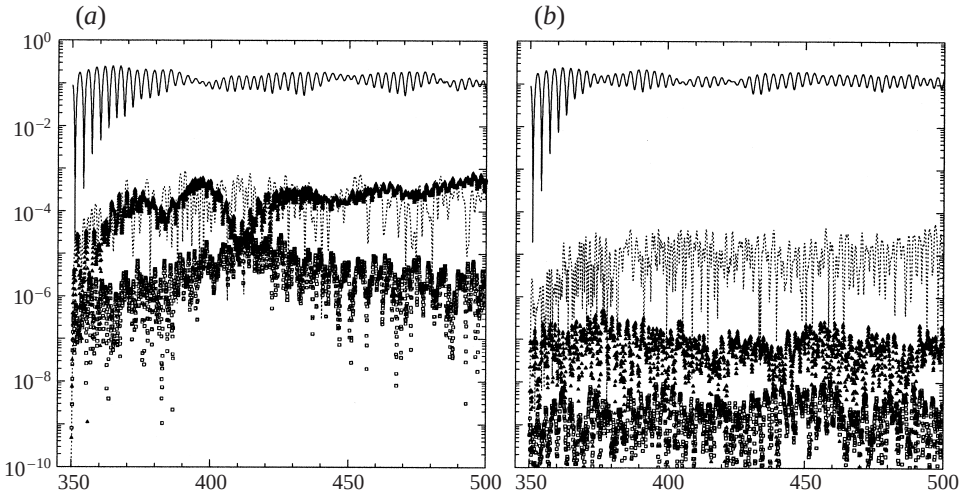

FIGURE 15. Cable (*a*) and beam (*b*): time-history of the (square) amplitude of the first four modes of cross-flow displacement. First mode is solid line, second mode is dashed line, third mode is solid triangles and fourth mode is open squares.

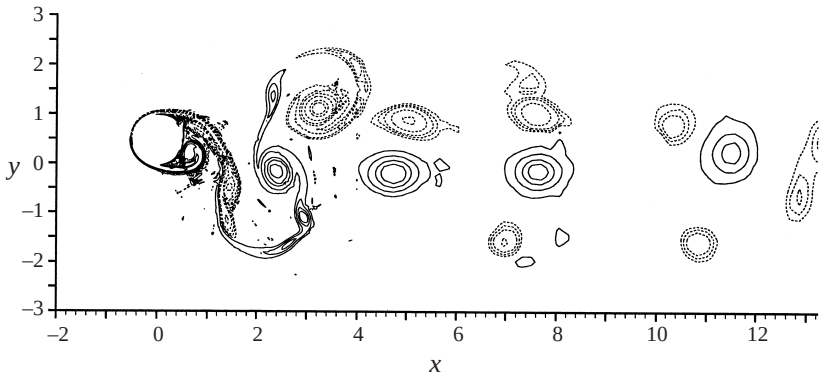

FIGURE 16. Vorticity contours at $t \approx 122$ (two-dimensional simulation, $Re = 1000$). Only the near wake is shown for clarity.

cylinder.) In figure 16 we plot the instantaneous vorticity field at non-dimensional time $t \approx 122$, which corresponds to approximately five shedding cycles after the initial state; at that instance the lift coefficient and the motion are out of phase by 180°. We see that the near wake corresponds to a $2P$ pattern, the intermediate wake to a $P+S$ pattern, and the far wake to a $2S$ (not shown here, see Evangelinos 1999). Here we use the terminology introduced by Williamson & Roshko (1988) to characterize the shedding patterns in flow past an oscillating cylinder, with $2S$ being the standard von Kármán mode, $2P$ a pattern with two pairs of vortices per shedding cycle, and $P+S$ a pattern of three vortices per shedding cycle. In figure 17 we plot vorticity contours at $t \approx 136$, which corresponds to a cylinder motion in phase with the lift and a relatively large amplitude of oscillation (see figure 2). We see that the near wake exhibits $P+S$ patterns (two large vortices plus a small vortex always shed to the same side every cycle – notice the small vortices at about $(3, -1.5)$ and $(7, -1)$);

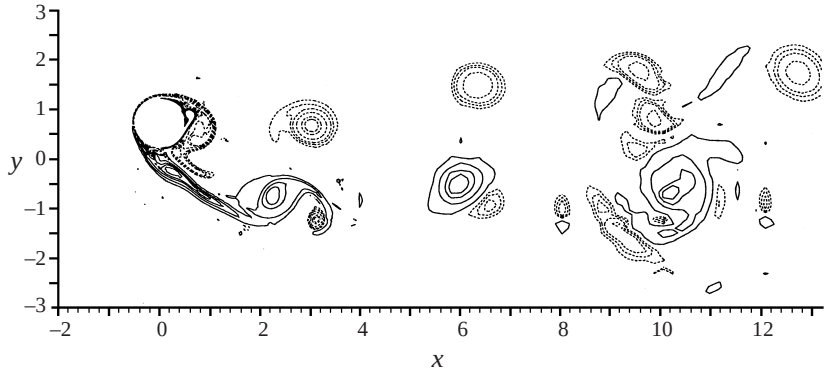

FIGURE 17. Vorticity contours at $t \approx 136$ (two-dimensional simulation, $Re = 1000$). Only the near wake is shown for clarity.

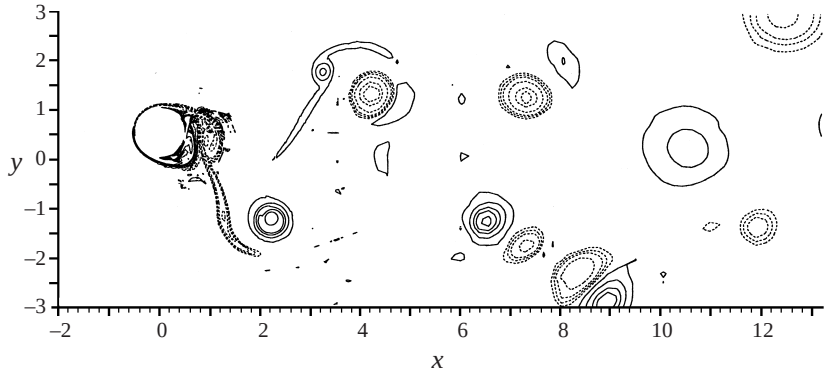

FIGURE 18. Vorticity contours at $t \approx 176$ (two-dimensional simulation, $Re = 1000$). Only the near wake is shown for clarity.

the vortex street becomes unstable beyond $x/d \approx 10$. In the far wake we observe a mixed response downstream consisting of a $2P$ pattern (at $20d$ and $30d$) and a $P + S$ pattern (at $40d$) (see Evangelinos 1999). Finally, in figure 18 we plot vorticity contours representative of the asymptotic state at $t \approx 176$. We see that a $2P$ shedding pattern emerges in the near wake, followed by a $2S$ pattern, before the vortex street becomes unstable farther downstream.

The coexistence of such mixed responses, revealed in our simulations, has also been discovered by Ongoren & Rockwell (1988) in their systematic experimental investigation of cylinders subject to prescribed oscillations. At low Reynolds number, $Re = 200$, independent simulations by Newman & Karniadakis (1995) and Meneghini, Saltara & Bearman (1997) have shown that the standard $2S$ pattern is maintained for the oscillating cylinder, similar to the stationary cylinder but with a larger lateral vortex spacing. At Reynolds number $Re = 500$ we found in our simulations (Evangelinos 1999) that at lock-in a $P + S$ shedding pattern prevails, which may result in a symmetry-breaking bifurcation of the motion. However, at states somewhat farther from the resonant state the $2S$ mode re-appears and symmetry is restored.

The amplitude of the oscillation is low for all the cases reported except from the short interval between time $t \approx 130$ and $t \approx 145$ in figure 2. These results agree with the results of Saltara *et al.* (1998), who have also computed similar values for

the amplitude of the motion and have observed both $2P$ and $2S$ shedding patterns depending on the value of the reduced velocity. The small amplitudes observed in the two-dimensional simulations suggest that the resonant branch simulated is actually the lower one as observed in the experiments of Brika & Laneville (1993) and Khalak & Williamson (1996). The simulations show that in this case a $2P$ shedding pattern prevails in the near wake consistent with the experimental observations. However, the $P+S$ flow pattern simulated in figure 17, which is only stable for a short time interval, corresponds to the upper branch of the resonant curve, for which a $2S$ pattern was assigned in the experiments of Brika & Laneville (1993) and Khalak & Williamson (1996). The reason for that discrepancy between simulation and experiment is that the third vortex present in the $P+S$ pattern is so weak that it diffuses very quickly and disappears almost immediately after the first pair of vortices, so it is very hard capture in the experiments. At Reynolds number $Re = 500$ this $P+S$ pattern survives and is convected a large distance downstream before the vortex street breaks down at about $30d$ (see Evangelinos 1999).

5.2. *Low-Re vs. high-Re flow past a rigidly moving cylinder*

The flow patterns in the three-dimensional simulations presented are substantially different from the two-dimensional ones not only for flows past a cable or a beam where the oscillation amplitude varies along the span, but also for the freely moving rigid cylinder.

To contrast low Reynolds number shedding with shedding at $Re = 1000$ we first plot in figure 19 pressure isocontours at $Re = 300$ for the freely oscillating rigid(ly moving) cylinder. We see that shedding is parallel in the near wake and that the first strong interaction occurs at a location $x/d \approx 10$. The near wake also appears two-dimensional up to that location. The corresponding shedding pattern is of the type $2S$ as in the low Reynolds number two-dimensional simulations.

At $Re = 1000$ the vortex tubes shown clearly in the low Reynolds number simulations are very deformed and are only visible in the very near wake. For the stationary cylinder (not shown here) the shedding is nominally parallel, although there is substantial three-dimensional structure in the form of small cells along the span. For the rigid freely oscillating cylinder shown in figure 20 shedding is also parallel, and by examining several slices of the flow along the span we identify a $2P$ pattern. Therefore, there is a switch from the $2S$ mode to a $2P$ mode as the Reynolds number increases, similar to the qualitative change in the two-dimensional simulations, and in accord with the visualizations of Sheridan *et al.* (1998).

5.3. $Re = 1000$ *flows past flexible cylinders*

In figure 21 we plot similar pressure contours for flow past a cable at $Re = 200$. In this case an oblique shedding pattern is present, which is caused by the travelling wave along the cable as shown also in Newman & Karniadakis (1997). The angle of the oblique shedding with respect to the axis of the cable is approximately 18°. Notice that the direction of the travelling wave, and thus of the oblique shedding, depends on the initial conditions; for example, different initial conditions may result in oblique shedding at -18°. Although not very clear, the shedding pattern appears to be of $2S$ type.

For the beam and the cable the vortex shedding at $Re = 1000$ has changed significantly compared to the low Reynolds number states. In figure 22 we plot pressure isocontours of the flow past a beam. We see that part of the wake corresponds to parallel shedding, similar to the rigid cylinder, and part corresponds to oblique

FIGURE 19. Rigidly moving cylinder at $Re = 300$: pressure isocontours at values -0.3 and -0.4. View facing the inflow from the side (flow is in the direction of the positive x-axis).

shedding at an angle of about 30°. The same mixed shedding pattern is observed for cables as shown in figure 23, where we plot pressure contours at the same time instance as the beam ($t = 508.09$). The oblique shedding is at a different angle (approximately 40° instead of 30) when compared to the beam. This underlines the importance of the structure type, which is the only difference between these cases. We recall that spectra taken for the beam and cable in the near wake are almost identical at the small scales but that differences appear in the autocorrelation functions. We see from the flow visualizations here and the spectra in figures 13 and 14 that statistical differences between the cable and the beam flows are substantially smaller than instantaneous differences or real flow structures.

The parallel-oblique pattern alternates from side to side along the span. In figure 24 we plot pressure contours again for the cable at a different time instance ($t = 487.34$) for which the cable is approximately in anti-phase with the cable at time $t = 508.09$ (see figure 23). We see that the parallel and oblique shedding patterns are on opposite sides in the two plots. This behaviour is also seen clearly for the beam (see figure 25 for a different angle of view). These as well as other flow visualizations not shown here suggest that the onset of oblique shedding coincides with the node which is travelling along the span. This creates a discontinuity in phase or a vortex dislocation (see Williamson 1996), which causes vortex filaments to turn with respect to the axis of the cable resulting in oblique shedding. These vortex filaments produce patterns similar to what have been termed phase shocks by Miller & Williamson (1994) who have created such structures experimentally using variable suction at the ends of a stationary cylinder. There is, however, a difference with the structures in

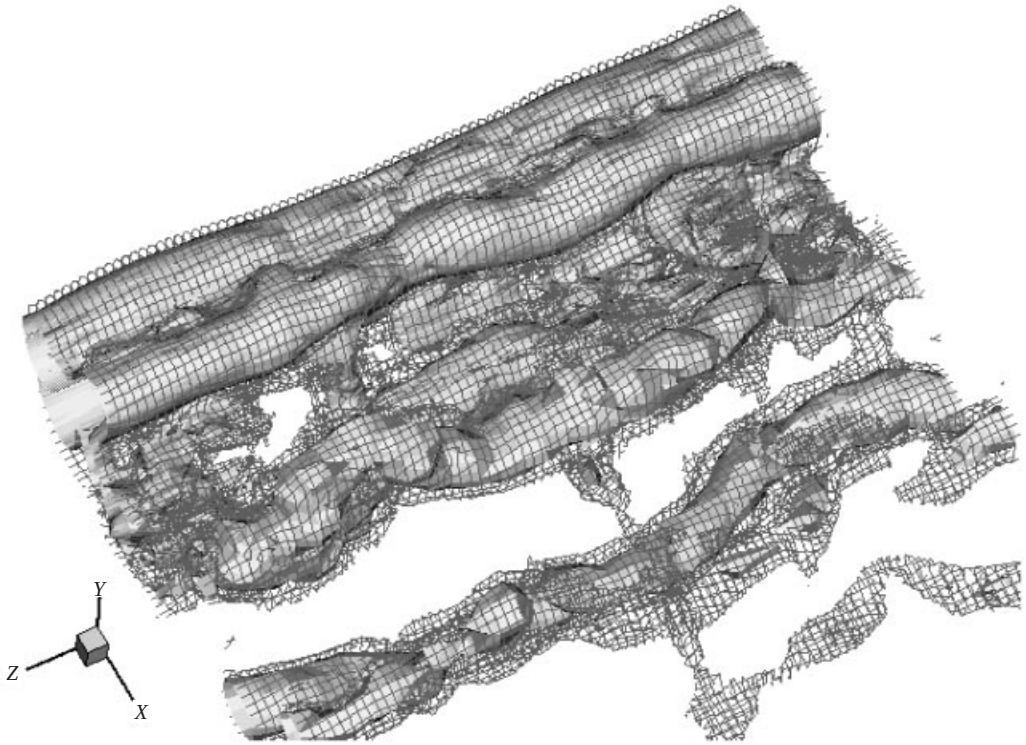

FIGURE 20. Rigidly moving cylinder at $Re = 1000$: pressure isocontours at values -0.3 and -0.2. View facing the inflow from the side.

our visualizations: unlike the experiment of Miller & Williamson (1994) where the discontinuity point is fixed, here it coincides with the node, which is moving with the phase speed along the span of the cable or beam. In the experiments with the stationary cylinder, therefore, the inclined vortex filaments are located towards one side of the cylinder, whereas in the cable or beam simulations the inclined filaments alternate sides.

The form of the shedding patterns is important as it is directly related to the forces on the structure. For example, examination of the instantaneous lift force spatial distribution shows that the maximum of lift coefficient corresponds to oblique shedding downstream. This is clearly shown by plotting the lift coefficient on the cable in figure 26 and marking the locations $t = 508.09$ and $t = 487.34$ corresponding to visualizations in figures 23 and 24, respectively.

A fundamentally different pattern is produced if the endpoints of the flexible cylinder in the span are pinned. In this case, a standing wave describes approximately the motion of the flexible cylinder. In figure 27 we plot instantaneous pressure contours for this flow at four consecutive time instants. The shedding patterns for this case are different from before, as the vortex tubes shed off the cylinder are bent towards the flow direction with fixed vortex dislocations at the two fixed nodes along the span. These flow structures appear to be a higher-Re 'relative' of the three-dimensional staggered pattern of lambda-type vortices observed in low-Re simulations (Newman & Karniadakis 1995, 1996, 1997).

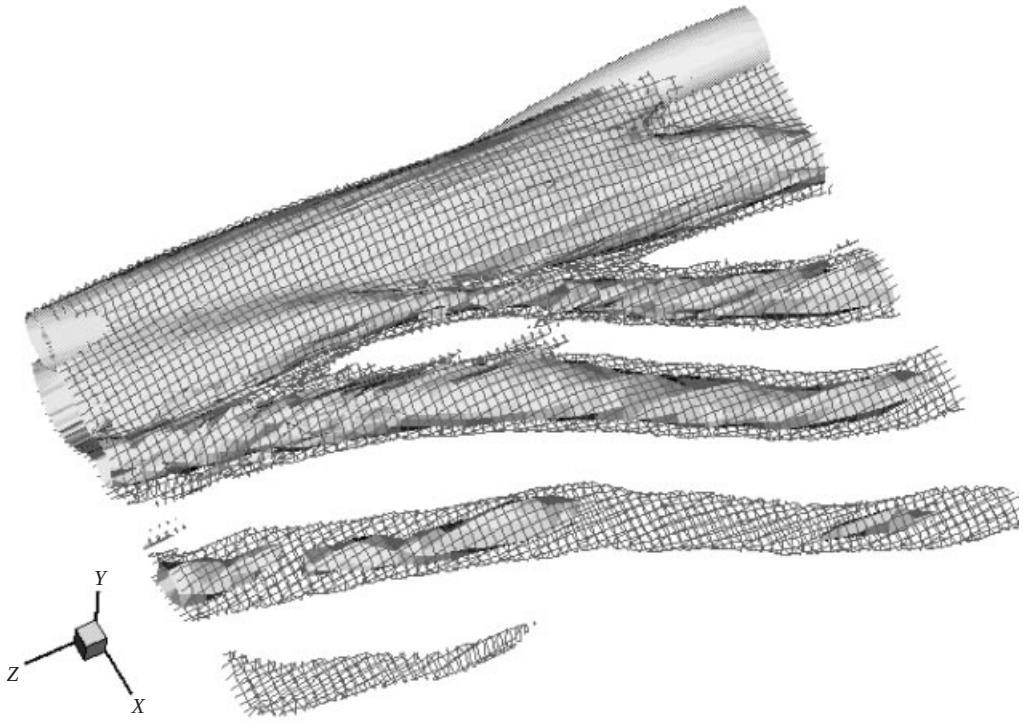

FIGURE 21. Cable at $Re = 200$: pressure isocontours at values -0.3 and -0.35. View facing the inflow from the side.

6. Summary and discussion

In this paper we have investigated the flow past rigidly moving and flexible cylinders subject to vortex-induced vibrations in the lock-in regime. We chose to perform all simulations at $Re = 1000$ as this corresponds to an order of magnitude increase compared to our previous studies (Newman & Karniadakis 1997) and at the same time the corresponding flow exhibits a turbulent wake. In addition, with this choice we can keep the expense of the computations reasonable and still maintain very high numerical accuracy. As regards the aspect ratio value of $L/d = 4\pi$, its selection represents a reasonable choice dictated by physical reality (see Vandiver 1991) and computational feasibility. Aspect ratio effects have already been studied previously in Newman & Karniadakis (1997) (where the aspect ratio was varied up to a value of 200 at $Re = 100$); more recent studies at $Re = 1000$ can be found in Evangelinos, Lucor & Karniadakis (1999) (where an aspect ratio of 378 was used). Due to the periodic boundary conditions we employ, the physical system that we consider corresponds to a long cylindrical structure having one of its high modes locked-in with the flow vortex shedding. The wavelength of the locked-in mode is then determined from the assumed aspect ratio and the structural parameters. In the case of the pinned endpoint simulations, the equivalent physical system would be a very long cylinder held in place by a periodic array of supports, a distance L apart.

Despite such simplifications the coupled flow–structure system exhibits quite complex dynamics, in agreement with the physical observations. In particular, we found

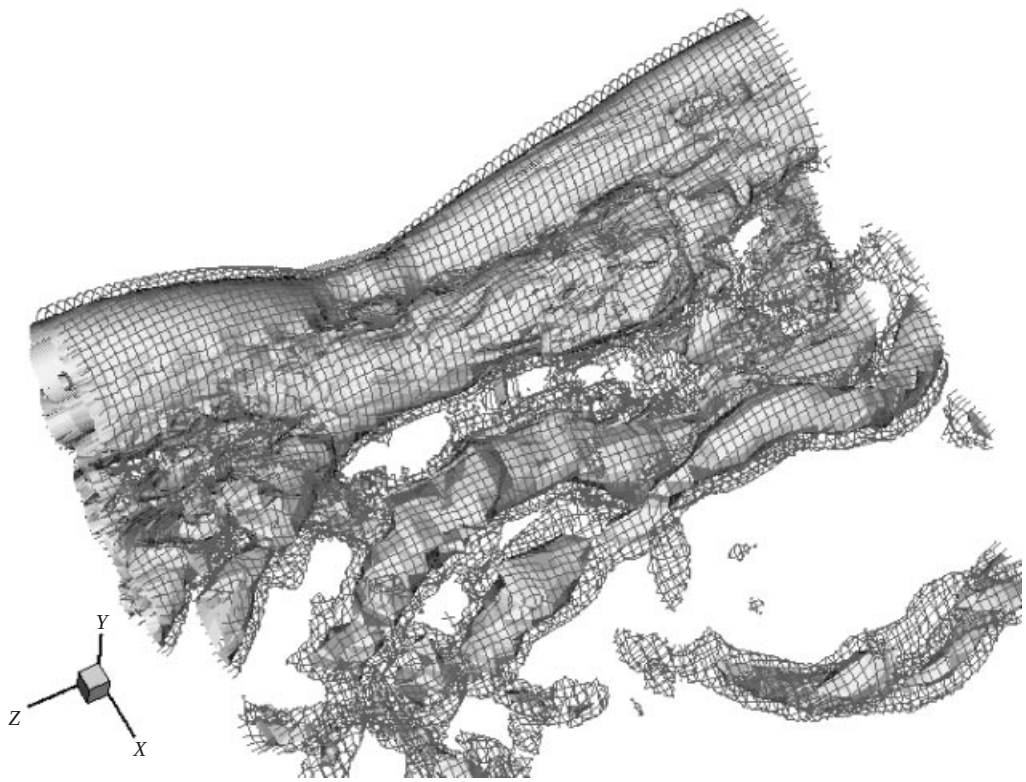

FIGURE 22. Beam at $Re = 1000$: pressure isocontours at values -0.25 and -0.18 ($t = 508.09$). View facing the inflow from the side.

that the amplitude of the oscillation of the structure increases to a value of about $1d$ (and asymptotically stays around $0.9d$) if the cylinder is flexible with freely moving endpoints. For a rigid cylinder the amplitude was found to be about $0.75d$. The cases with pinned endpoints gave us amplitudes even higher than $1d$. This kind of response should be contrasted with the value of $0.5d$–$0.6d$ obtained in the laminar. Such Reynolds numbers effects have recently been quantified in experimental studies (see Ching *et al.* 1998) but at a higher Reynolds number. The two-dimensional simulations predict an amplitude similar to the laminar flow, i.e. of the order of $0.5d$–$0.6d$ even at $Re = 1000$. A correlation between the cross-flow displacement and lift forces phase difference and the magnitude of the lift forces was observed and contrasted to results from two-dimensional simulations.

We observed two different types of cylinder oscillations, the first resembling a travelling (progressive) wave when the endpoints were free to move, and the second resembling a standing wave when the endpoints were pinned. Asymptotically, the maximum cylinder displacement is about $0.9d$ in the travelling wave case and $1.1d$ in the standing wave case. The root-mean-squared lift coefficient is about 0.8 for both cases but slightly larger in the case of the standing wave.

We simulated our structure not only as a cable but also as a beam, i.e. a structure with non-negligible bending stiffness, and compared the beam–flow response with a cable–flow response. We found that at low Reynolds number in the laminar regime the responses are identical but at $Re = 1000$ there are significant differences both in the flow structure and the dynamics of the cylinder. It is clear that in a multi-

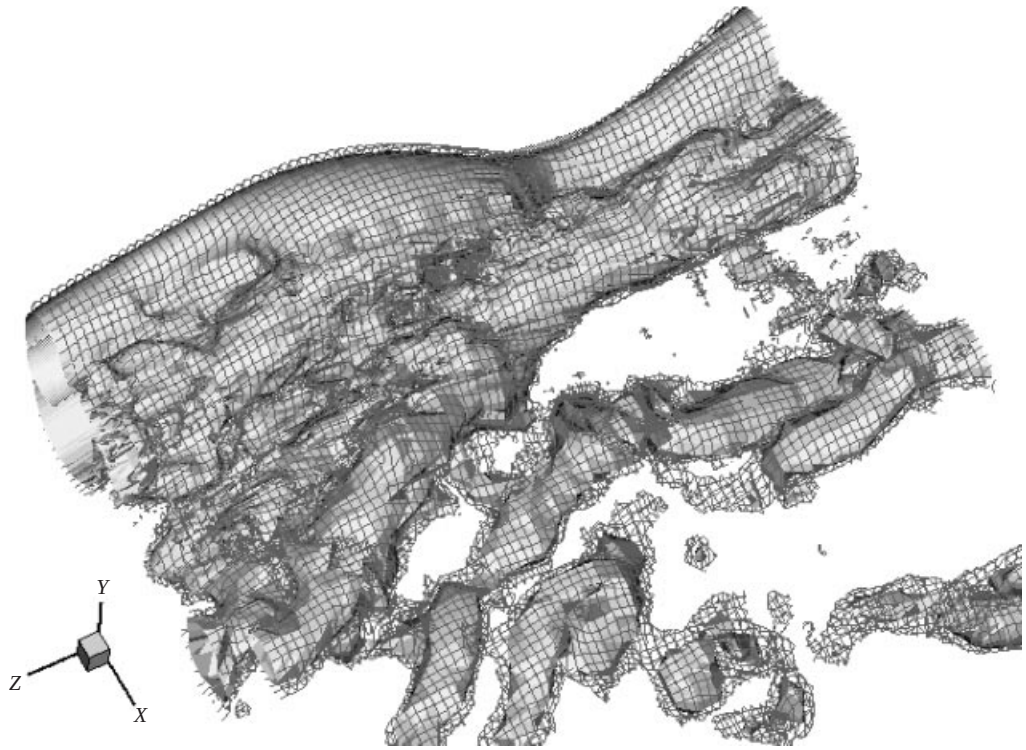

FIGURE 23. Cable at $Re = 1000$: pressure isocontours at values -0.15 and -0.12 ($t = 508.09$). View facing the inflow from the side.

modal response away from a lock-in state such differences will be even larger. The autocorrelation function for the velocity components in the wake of a beam appears to be in-between the cases of the wake behind a rigidly moving cylinder and that behind a cable. However, despite such differences in large scales there is a remarkable statistical similarity in the small scales as exemplified by comparisons of frequency spectra between the cable–flow and the beam–flow systems.

It has been suggested by Khalak & Williamson (1996) that the two-dimensional simulations capture the lower branch of the resonant curve, which corresponds to a $2P$ type shedding pattern according to their observations and in agreement with the visualizations of Brika & Laneville (1993). We re-examined this hypothesis in the current investigation and we found it to be true at $Re = 1000$, but at lower Reynolds number a different shedding pattern emerged of the standard $2S$ type or the more unusual $P + S$ type. This latter type of shedding was also present in the $Re = 1000$ simulations but only for a brief transient period of about two to three shedding cycles resulting in a higher amplitude of oscillation. We found that the specific shedding pattern sustained depends not only on the Reynolds number but also on the specific value of the reduced velocity even within the lock-in region; this was also observed in independent two-dimensional simulations by Saltara *et al.* (1998).

The three-dimensional shedding patterns are substantially different even for the case of a rigid cylinder that experiences the same displacement along all the points in the span. At $Re = 1000$ the flow is strongly three-dimensional although nominally parallel shedding prevails in the near wake but with a spanwise distribution of phase

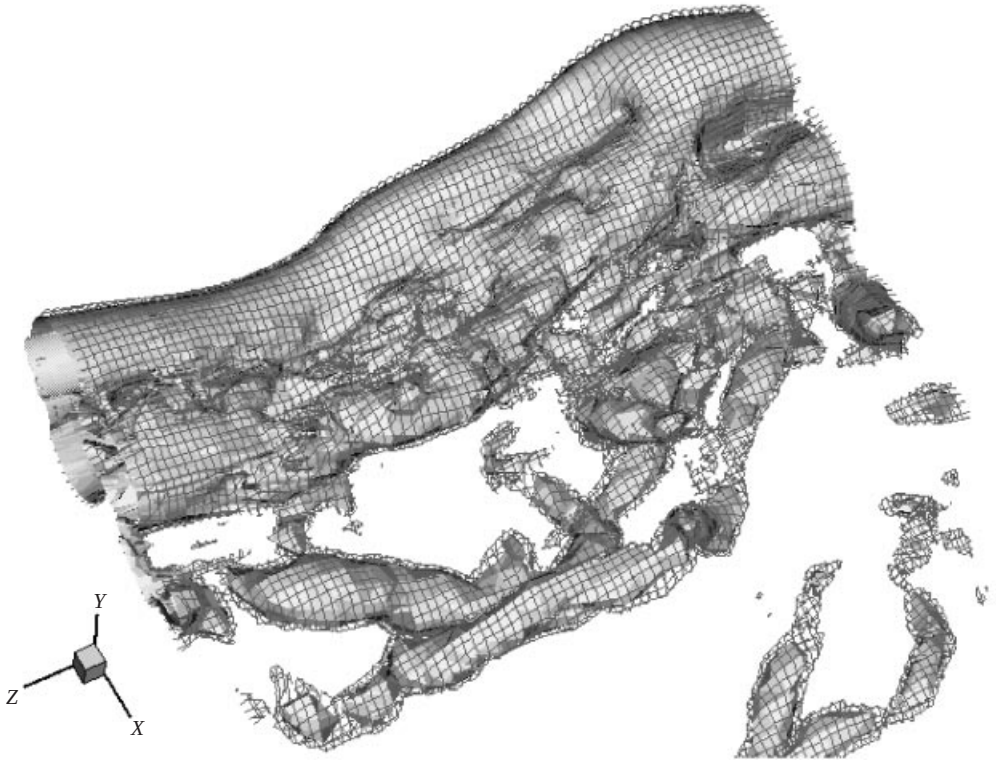

FIGURE 24. Cable at $Re = 1000$: pressure isocontours at values -0.15 and -0.12 ($t = 487.34$). View facing the inflow from the side.

difference between the motion and the wake of about $\pm 10^{\circ}$. For flexible cylinders, their modulated travelling wave response causes oblique shedding patterns as in the low Reynolds number regime (Newman & Karniadakis 1997). At $Re = 1000$ these patterns coexist with parallel shedding, and the two patterns alternate sides (along the span) during one shedding cycle. This periodic change from oblique to parallel shedding corresponds to a large variation of the lift forces along the span, so by knowing the near-wake shedding pattern we can infer the lift coefficient distribution on the cylinder. A similar mixed parallel/oblique shedding pattern has also been visualized at a lower Reynolds number in the experiments of Van Atta *et al.* (1988). Such large-scale phenomena characterized as phase shocks (see Miller & Williamson 1994) can be described by a low-dimensional model such as the Ginzburg–Landau equation (see Albarede & Monkewitz 1992).

Unfortunately, currently there are no available complete experimental data to substantiate the new findings presented here regarding both the statistical quantities we computed as well as the flow structures we observed. It remains still an open question, assuming that the two-dimensional simulations capture the lower branch of the resonant curve, if the three-dimensional simulations capture the upper branch

FIGURE 25. Beam at $Re = 1000$: (*a*) pressure isocontours at values -0.24 and -0.18 ($t = 490.09$); (*b*) pressure isocontours at values -0.24 and -0.18 ($t = 532.09$). Views facing the outflow from the side (flow is in the direction of the positive x-axis).

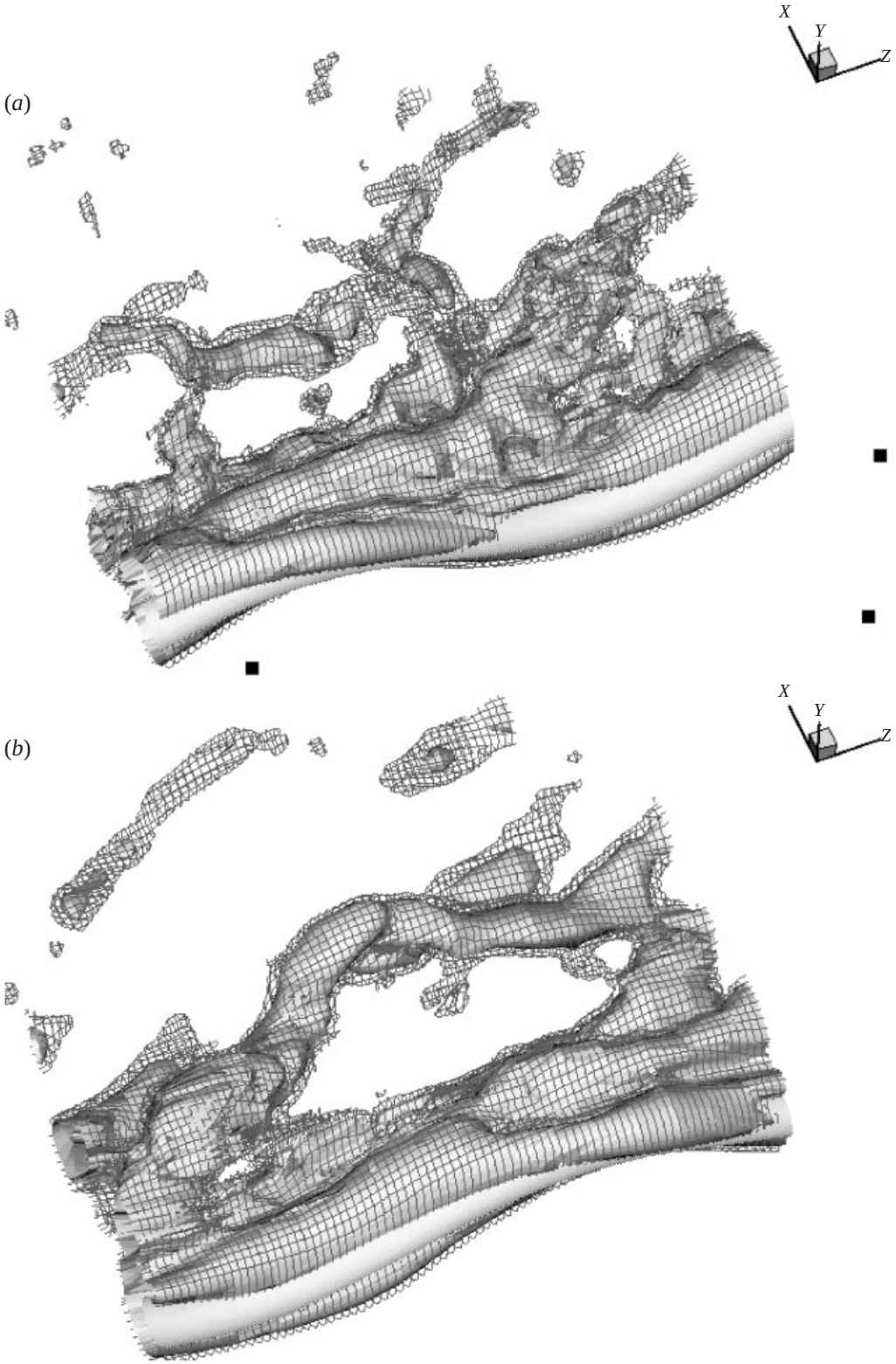

FIGURE 25. For caption see facing page.

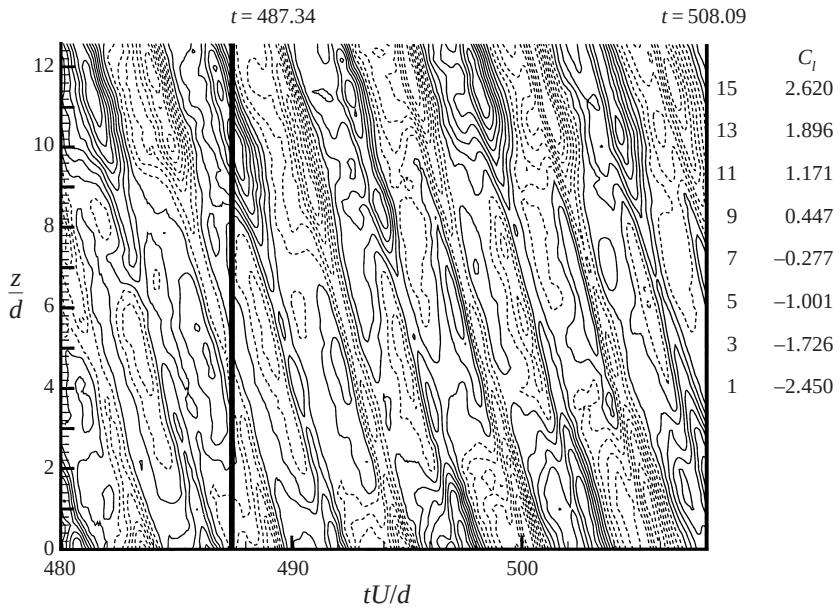

FIGURE 26. Cable at $Re = 1000$: lift coefficient along the span versus time.

given the larger values of the cross-flow displacement. The $2S$ shedding pattern assigned to the upper branch by Khalak & Williamson (1996) and by Brika & Laneville (1993) does not seem to be a unique feature of that state. The current simulations suggest that patterns of the type $P + S$ may also be associated with the upper branch; however these are difficult to discern experimentally due to the much weaker "third" vortex of the group and its fast dissipation.

This work was supported partially by ONR and DOE. The computations were performed on the Cray T3E at NAVO, on the IBM SP2 at Maui High Performance Computing Center (MHPCC), and at Brown University. We would like to thank Dr Tim Warburton and Dr Ma Xia for their help with the $\mathcal{N}\epsilon\kappa\mathcal{T}\alpha r$ code. We also want to thank Dr J. Meneghini for suggestions regarding the flow visualizations of the two-dimensional simulations.

Appendix A. Numerical formulation and validation

To solve the three-dimensional Navier–Stokes equations, the new code $\mathcal{N}\epsilon\kappa\mathcal{T}\alpha r$ (see Warburton 1998) is used. It is based on hierarchical spectral/hp expansions on hybrid subdomains, i.e. triangles and quadrilaterals as shown in figure 28. Jacobi polynomials of mixed weights are used for the trial basis that form tensor products of generalized type. The nonlinear products are handled using effectively a super-collocation approach followed by a Galerkin projection (Karniadakis & Sherwin 1999). Each element can accommodate variable spectral order so that regions of different dynamics are treated accordingly as shown in the figure. This is accomplished by arranging the trial basis in terms of vertex, boundary and bubble modes and ensuring matching of the boundary modes, thus satisfying the C^0 continuity condition required in the Galerkin formulation.

The parallel implementation is based on a framework similar to that described earlier in Crawford *et al.* (1996). Two-dimensional elements are used to discretize

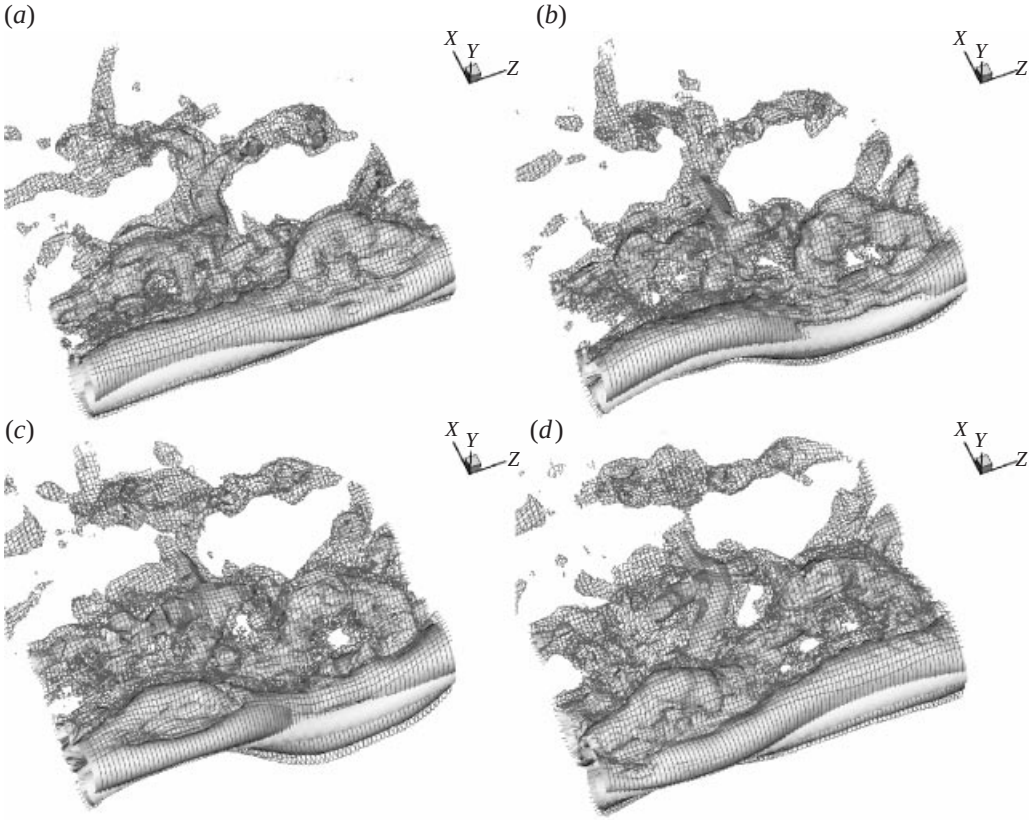

FIGURE 27. Standing wave response for a beam with pinned endpoints at $Re = 1000$: pressure isocontours at values -0.1 and -0.2. The different snapshots correspond to times one-fifth of the shedding cycle apart (*a*, *b*, *c*, *d*). Views facing the outflow from the side (flow is in the direction of the positive x-axis).

the (x, y)-planes, while a Fourier expansion is used in the z-direction (i.e. along the cylinder axis) with a dealiasing $\frac{3}{2}$ rule. A Newmark integration scheme (see Hughes 1987; Newman 1996) is used to solve for the structure.

The computational domain for the (x, y)-plane used for the $Re = 1000$ (as well as any $Re = 500$) calculations extends $69d$ (cylinder diameters) downstream, and $22d$ in front, above and below the cylinder. For three-dimensional simulations the spanwise length is $L/d = 4\pi$. A $K = 1018$ element hybrid mesh was used for the $Re = 1000$ calculations (see figure 28), with a slightly smaller $K = 988$ element one for any $Re = 500$ ones. The polynomial order used varied across the domain as shown in figure 28. Two different resolutions were used in the z-direction for all cases: 32 z-planes (16 independent Fourier modes) for the stationary and rigidly moving cylinder simulations and 64 z-planes for cables and beams; a $\frac{3}{2}$ de-aliasing rule was always used. For the largest cases this meant more than 19 million degrees of freedom over the three velocity fields and pressure. For all but the stationary cylinder calculations (which can sustain twice the timestep size) CFL limitations force a non-dimensional time step of $\Delta tU/d = 0.0005$ to be used giving over 10 000 time steps per shedding cycle. Simulation runs were performed on 32 processors of a Cray T3E-900 and an IBM SP2/160MHz P2SC, used up approximately 200MB per processor and took close to 12 seconds per time step in the case of the flexible cylinders.

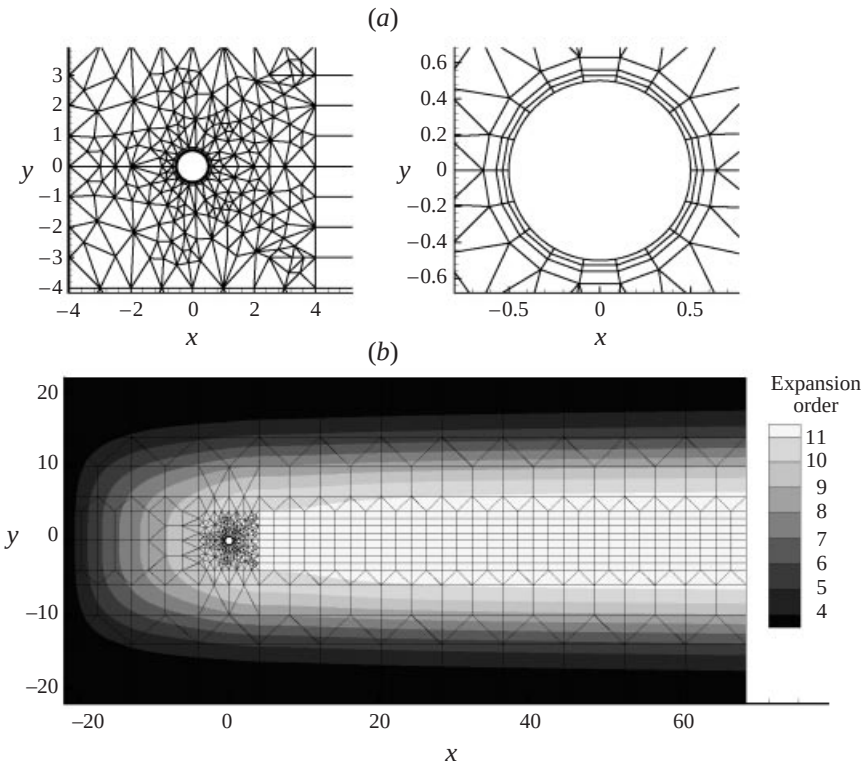

FIGURE 28. Hybrid grid in the (x, y)-plane; Fourier expansions are used in the periodic spanwise direction. Close-up of the discretization around the cylinder (*a*), and colour contours of the variable expansion order (polynomial order + 1) per element (*b*).

Validation of the new code $\mathcal{N}\boldsymbol{\epsilon\kappa}\mathcal{T}\boldsymbol{\alpha r}$ was accomplished by repeating laminar flow simulations as in Newman & Karniadakis (1997) and also by comparing with experimental results. For the moving domain the results of the boundary-fitted coordinate formulation were compared (see Evangelinos 1999) to a different arbitrary Lagrangian–Eulerian (ALE) formulation (Warburton & Karniadakis 1997) and very good agreement was obtained for identical boundary conditions. A systematic validation study was performed for the stationary turbulent wake at $Re = 1000$ and comparisons were made with earlier simulations using mortar spectral element simulations (Henderson & Karniadakis 1995) and also accepted experimental results (Norberg 1994) (and references therein). A summary of this comparison is shown in table 1, where we see that the current simulation results are much closer to the experimental results than the computations reported in Henderson & Karniadakis (1995). A breakdown of the contribution to lift and drag of pressure- and viscosity-generated forces is shown in figure 29. We have used these measures to conduct refinement studies as well as to choose the size of the computational domain.

Appendix B. Three-dimensional simulations: visualization approach

$\mathcal{N}\boldsymbol{\epsilon\kappa}\mathcal{T}\boldsymbol{\alpha r}$ uses unstructured and hybrid domains, which lead to a distribution of output data in a very non-uniform grid. Most available visualization packages suffer

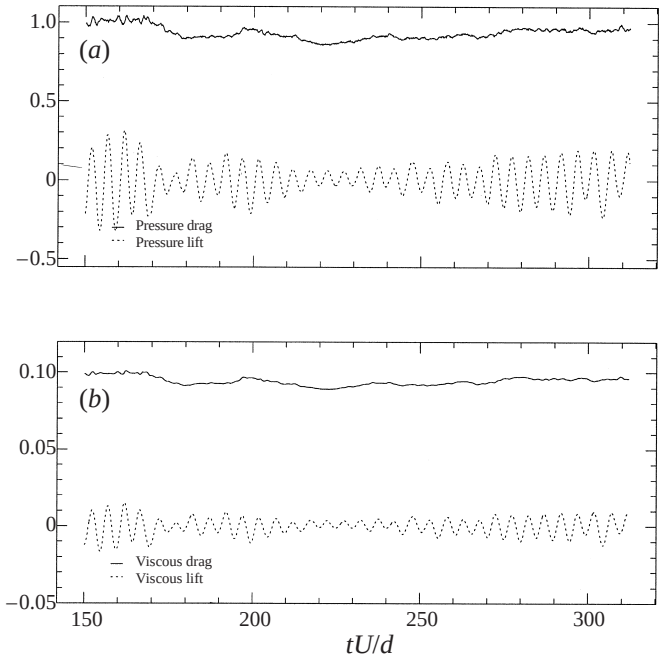

FIGURE 29. Fluctuating lift and drag coefficients for flow past a stationary cylinder at $Re = 1000$: pressure forces (*a*) and viscous forces (*b*).

	St	$-C_{pb}$	C_d	$\acute{C}_d$	$\acute{C}_l$
2D Henderson & Karniadakis (1995)	0.237	1.6944	1.5144	0.1594	1.0494
2D current	0.238	1.7138	1.5406	0.1715	1.0696
3D Henderson & Karniadakis (1995)	0.211	1.1225	1.1999	0.0491	0.2052
3D current	0.202	0.8429	1.0192	0.0348	0.0991
Experiment	0.21	0.8	1.0	?	?

TABLE 1. Comparison of simulation results with experimental results for flow past a stationary cylinder at $Re = 1000$. St is the Strouhal frequency, C_{pb} is the base pressure coefficient, C_d is the mean drag coefficient, $\acute{C}_d$ is the standard deviation in the drag coefficient and $\acute{C}_l$ is the standard deviation in the lift coefficient.

from severe accuracy degradation when handling data in non-uniform grids. To this end, we first interpolate the output of $\mathcal{N}\boldsymbol{\epsilon\kappa}\mathcal{T}\boldsymbol{\alpha r}$ using spectral interpolations on a uniform grid by respecting the dynamic changes in the geometry, and subsequently we perform the visualizations.

We are interested in studying the near-wake vorticity dynamics and so vorticity visualization is a standard approach used. While this is useful and admits a fairly simple interpretation in two dimensions, in three dimensions vorticity visualizations are substantially more difficult to perform and to interpret. For example, if vorticity magnitude is used as a scalar quantity to visualize the near wake in flow–structure interactions, important details of the dynamics cannot be presented. Instead, we can use isosurfaces of pressure at appropriate levels to visualize details of the wake. A

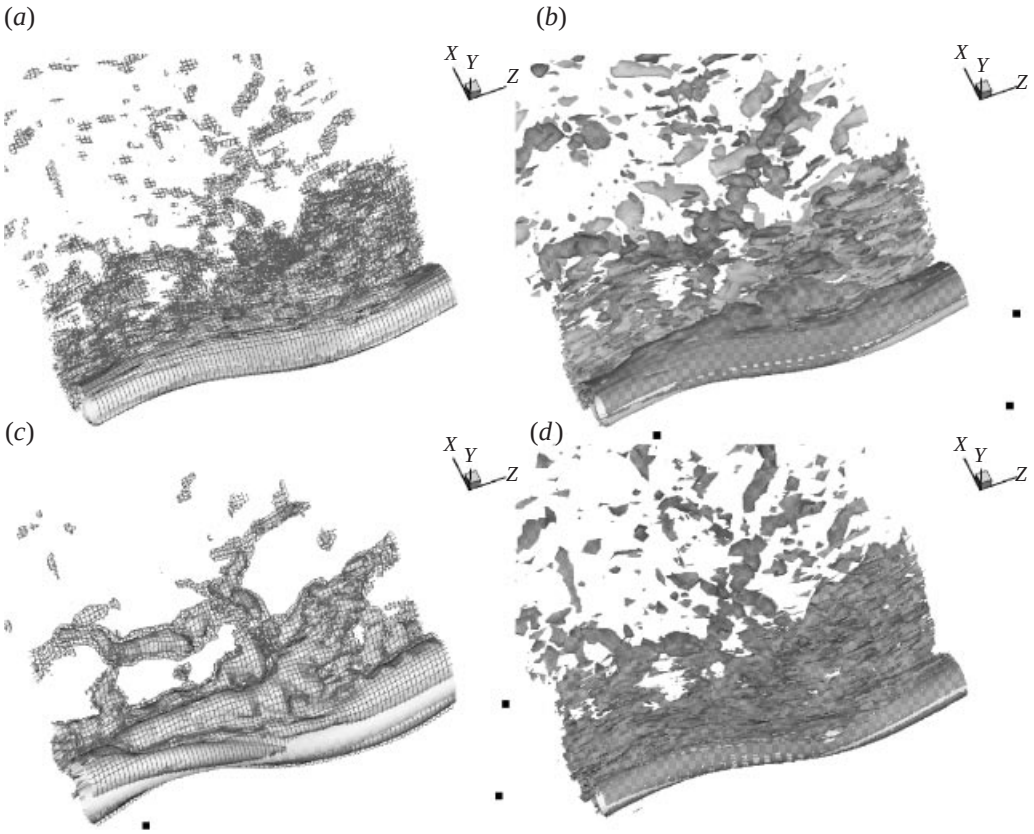

FIGURE 30. DNS of flow past a flexible beam at $Re = 1000$. (*a*) Total vorticity magnitude at levels 3.0 and 5.5; (*b*) spanwise vorticity at -1.7 and 1.7; (*c*) pressure isosurfaces at -0.18 and -0.24. (*d*) isocontour at -1.3 of the second largest eigenvalue of the velocity gradient tensor using the technique of Jeong & Hussain (1995). All values are non-dimensionalized with respect to the flexible cylinder diameter and the freestream velocity.

more accurate approach is to find the vortex cores using the approach pioneered by Jeong & Hussain (1995) based on the eigenvalues of the velocity gradient tensor, but this is rather costly.

To contrast the visualization results obtained using the different methods, we plot in figure 30 isosurfaces of vorticity magnitude at two different values, and pressure isosurfaces. In particular, we employ a *solid surface* at a minimum (negative value) and another *grid surface* at a value slightly above the previous one. To demonstrate that the iso-pressure surfaces so tracked are representative of the corresponding vorticity dynamics, we also plot in figure 30 a similar plot of the spanwise vorticity following the same two-surface tracking approach, as before. We see that indeed the pressure isosurface and the spanwise vorticity isosurfaces present the same instantaneous picture in the near wake. We also include an isocontour plot following the technique of Jeong & Hussain (1995), which shows the resemblance with the other plots but it is not as informative as the pressure isosurface plot. In general, it is more efficient to follow pressure isosurfaces than vorticity (which needs to be computed at post-processing) isosurfaces, so this is the approach we employ.

REFERENCES

Albarede, P. & Monkewitz, P. 1992 A model for the formation of oblique shedding patterns and 'chevrons' in cylinder wakes. *Phys. Fluids* A **4**, 744.

Alexander, C. 1981 The complex vibrations and implied drag of a long oceanographic wire in crossflow. *Ocean Engng* **8**, 379–406.

Bearman, P. 1984 Vortex shedding from oscillating bluff bodies. *Ann. Rev. Fluid Mech.* **16**, 125–177.

Blackburn, H. & Karniadakis, G. 1993 Two- and three-dimensional simulations of vortex-induced vibration of a circular cylinder. In *Proc. 3rd Intl Offshore and Polar Engng Conf., Singapore*, vol. 3, p. 715.

Blevins, R. 1990 *Flow Induced Vibration*. Van Nostrand Reinhold.

Bloomfield, P. 1976 *Fourier Analysis of Time Series: An Introduction*. John Wiley & Sons.

Brika, D. & Laneville, A. 1993 Vortex-induced vibrations of a long flexible circular cylinder. *J. Fluid Mech.* **250**, 481–508.

Ching, A., So, R. & Zhou, Y. 1998 Measurements of the wake and transverse displacements of a flexible cylinder in a cross flow. In *Proc. ASME Fluids Summer Meeting, Conference on Bluff Body Wakes and Vortex-Induced Vibrations, Washington DC* (ed. P. W. Bearman & C. H. K. Williamson).

Crawford, C., Evangelinos, C., Newman, D. & Karniadakis, G. 1996 Parallel benchmarks of turbulence in complex geometries. *Computers Fluids* **25**, 677–698.

Evangelinos, C. 1999 Parallel simulations of vortex-induced vibrations in turbulent flow: Linear and non-linear models. PhD thesis, Division of Applied Mathematics, Brown University.

Evangelinos, C., Lucor, D. & Karniadakis, G. 1999 DNS-Derived force distribution on flexible cylinders subject to VIV. *J. Fluids Struct.* (to appear).

Feng, C. 1998 The measurement of vortex-induced effects in flow past a stationary and oscillating circular and D-section cylinders. Master's thesis, University of Britich Columbia, Vancouver, B.C., Canada.

Furnes, G. 1998 On marine riser responses in time and depth dependent flows. *Tech. Rep.* Norsk Hydro, Bergen, Norway.

Gharib, M., Gharib, M., Leonard, A. & Roshko, A. 1998 The absence of lock-in and the role of mass-ratio. In *Proc. ASME Fluids Engineering Division on Bluff Body wakes and Vortex-Induced Vibration, Washington DC*.

Griffin, O. 1992 Vortex-induced vibrations of marine structures in uniform and sheared currents. *NSF workshop on Riser Dynamics, University of Michigan.*

Henderson, R. & Karniadakis, G. 1995 Unstructured spectral element methods for simulation of turbulent flows. *J. Comput. Phys.* **122**, 191–217.

Hover, F., Grosenbaugh, M. & Triantafyllou, M. 1994 Calculation of dynamic motions and tensions in towed underwater cables. *IEEE J. Ocean. Engng* **19**, 449.

Hover, F., Techet, A. & Triantafyllou, M. 1998 Forces on oscillating uniform and tapered cylinders in crossflow. *J. Fluid Mech.* **363**, 97–114.

Hughes, T. 1987 *The Finite Element Method*. Prentice-Hall.

Jeong, J. & Hussain, F. 1995 On the identification of a vortex. *J. Fluid Mech.* **285**, 69–94.

Karniadakis, G. & Sherwin, S. 1999 *Spectral/hp Element Methods for CFD*. Oxford University Press.

Khalak, A. & Williamson, C. 1996 Dynamics of a hydroelastic cylinder with very low mass and damping. *J. Fluids Struct.* **10**, 455–472.

Mansy, H., Yang, P.-M. & Williams, D. 1994 Quantitative measurements of three-dimensional structures in the wake of a circular cylinder. *J. Fluid Mech.* **270**, 277–296.

Meneghini, J., Saltara, F. & Bearman, P. 1997 Numerical simulation of vortex shedding from an oscillating circular cylinder. In *Proc. 8th Intl Conf. on Computational Methods and Experimental Measurements, Rhodes, Greece, 1997.*

Miller, G. & Williamson, C. 1994 Control of three-dimensional phase dynamics in a cylinder wake. *Exps. Fluids* **18**, 26.

Newman, D. 1996 A computational study of fluid/structure interactions: flow-induced vibrations of a flexible cable. PhD thesis, Princeton University.

Newman, D. & Karniadakis, G. 1995 Direct numerical simulations of flow over a flexible cable.

In *Sixth Intl Conf. on Flow-Induced Vibrations, Imperial College, April 10–12, 1995* (ed. P. W. Bearman). Balkema.

Newman, D. & Karniadakis, G. 1996 Simulations of flow over a flexible cable: A comparison of forced and flow-induced vibration. *J. Fluids Struct.* **10**, 439–453.

Newman, D. & Karniadakis, G. 1997 Simulations of flow past a freely vibrating cable. *J. Fluid Mech.* **344**, 95–136.

Norberg, C. 1994 An experimental investigation of the flow around a circular cylinder: Influence of aspect ratio. *J. Fluid Mech.* **258**, 287–310.

Olinger, D. 1996 A low-order model for vortex shedding patterns behind vibrating flexible cables. *Phys. Fluids* **10**, 1953–1961.

Ongoren, A. & Rockwell, D. 1988 Flow structure from an oscillating cylinder – part 1: Mechanisms of phase shift and recovery in the near wake. *J. Fluid Mech.* **191**, 197–223.

Parkinson, G. 1989 Phenomena and modeling of flow-induced vibrations of bluff bodies. *Proc. Aerospace Sci.* **26**, 169–224.

Ramberg, S. & Griffin, O. 1976 The effects of vortex coherence, spacing, and circulation on the flow-induced forces on vibrating cables and bluff structures. *Naval Research Lab. Rep.* 7945.

Saltara, F., Siqueira, C., Meneghini, J. & Bearman, P. 1998 The simulation of vortex shedding from an oscillating circular cylinder with turbulence modeling. In *Proc. ASME Fluids Summer Meeting, Conference on Bluff Body Wakes and Vortex-Induced Vibrations, Washington DC* (ed. P. W. Bearman & C. H. K. Williamson).

Sheridan, J., Carberry, J., Lin, J.-C. & Rockwell, D. 1998 On the near-wake topology of an oscillating cylinder. *J. Fluids Struct.* **12**, 215–220.

Toebes, G. 1969 The unsteady flow and wake near an oscillating cylinder. *Trans. ASME: J. Basic Engng* **91**, 493–502.

Van Atta, C., Gharib, M. & Hammache, M. 1988 Three-dimensional structure of ordered and chaotic vortex streets behind circular cylinders at low Reynolds number. *Fluid Dyn. Res.* **3**, 127–132.

Vandiver, J. 1991 Dimensionless parameters important to the prediction of vortex-induced vibrations of long, flexible cylinders in ocean currents. *MIT Sea Grant Rep.* MITSG 91-93.

Vandiver, J. & Li, L. 1994 SHEAR7 Program theoretical Manual. *Tech. Rep.* MIT, Dept. Ocean Engineering, Cambridge, MA.

Warburton, T. 1998 Spectral/hp element methods on polymorphic multi-domains: Algorithms and applications. PhD thesis, Division of Applied Mathematics, Brown University.

Warburton, T. & Karniadakis, G. 1997 Spectral simulation of flow past a cylinder close to a free surface. In *Proc. Fluids Engineering Division Summer Meeting, Vancouver*. FEDSM97-3689.

Williamson, C. 1996 Vortex dynamics in the wake. *Ann. Rev. Fluid Mech.* **28**, 477–539.

Williamson, C. & Roshko, A. 1988 Vortex formation in the wake of an oscillating cylinder. *J. Fluids Struct.* **2**, 355–381.

Yoerger, D., Grosenbaugh, M., Triantafyllou, M. & Burgess, J. 1991 Drag forces and flow-induced vibrations of a long vertical tow cable – part 1: Steady-state towing conditions. *J. Offshore Mech. Arctic Engng* **113**, 117.